1 2  9 0

UNIVERSIDADE D
COIMBRA

Mohammadreza Shamshiri

INFLUENCE OF LASER STRUCTURAL PATTERNING ON THE TRIBOLOGICAL PERFORMANCE OF C-ALLOY TMD COATINGS

VOLUME 1

Dissertação no âmbito do Mestrado Conjunto Europeu em Tribologia de Superfícies e Interfaces orientada pelo Professor Doutor Albano Cavaleiro e apresentada ao Departamento de Engenharia Mecânica da Faculdade de Ciências e Tecnologia da Universidade de Coimbra

Julho de 2019

Acknowledgements

I would first like to express the deepest appreciation to my supervisor, Professor Albano Cavaleiro, for his patient guidance, valuable and constructive suggestions during the planning and development of this research work.

I would also like to offer my special thanks to Prof. Mitjan Kalin, the co-ordinator of TRIBOS program for providing me the opportunity of taking part in this program. In addition, I am particularly grateful to Prof. Ardian Morina (University of Leeds) and Prof. Bruno Trindade (University of Coimbra) for their support and patience.

Special thanks should be given to Dr. Todor Vuchcov, for his technical assistance, valuable comments and suggestions which have improved the quality of this thesis.

I would also like to extend my thanks to the staff of Instituto Pedro Nunes (IPN), especially Dr. Ana Manaia, and Physics department of the University of Aveiro for their help in running this work.

I express my gratitude to my parents for providing me with unfailing support and continuous encouragement throughout my years of study.

Above all I would like to thank my wife, Samaneh, for her love and constant support particularly during the last two years.

Abstract

Recent discoveries of self-lubricating of transition metal dichalcogenide (TMD) coatings have created a lot of excitements in this class of materials. The lubricious property of these coatings makes them a promising candidate for future applications in industries such as the polymer moulding, where the huge volume of materials is wasted, due to problems of mould release and fouling. Doping WS films by carbon using the sputtering techniques can result in an amorphous structure and decline the self-lubricious property in comparison with the pure WS_2 film. The aim of the present study is to improve the self-lubricity of a W-S-C coating using a laser treatment method. Various conditions for laser treatment such as different spots' patterns, power densities, duration of irradiation and so on, are employed to find the optimum results. The structure, morphology and mechanical properties of the treated coatings are analysed using SEM, Raman spectroscopy, X-ray diffraction and nanoindentation. In addition, a reciprocating ball-on-disk tribometer is employed for tribological characterization of the laser treated samples. It is concluded that the treatment using low laser power can cause WS_2 crystallization in the W-S-C coating and consequently improvement of tribological properties.

Keywords: Transition Metal Dichalcogenides, Laser, Magnetron spattering, Tribology

Contents

List of the figures

List of the tables

Chapter 1

1-Introduction

Rising consumption of infinite energy resources because of economic growth and finding out how to generate growth with fewer resources have become the crucial issues throughout the world. Scientists have been investigating energy dissipation and material loss, particularly in relation to friction and wear, for more than 300 years. In fact, about one-third of world energy resources in the present use, appears as friction in one form or another. These two concepts, namely friction and wear, are considerably connected with the field of science called tribology [1].

Tribology is the technology and science of interacting surfaces in relative motion. The word tribology is derived from the Greek word 'Tribos' which means rubbing, so tribology would be the science of rubbing. Estimates show that the ignorance of tribology in the U.S. results in losses, equal to about 6% of its gross national product or about $200 billion per year. Thus, saving energy and materials using reducing friction and wear is a beneficial solution, also resulting in an increased lifetime of components [2,3].

Using solid lubricants is one the effective solutions to reduce the coefficient of friction and wear. These lubricants could be very beneficial in the systems where oil lubrication is not possible as the vacuum applications or the sliding contacts where the presence of contaminants must be prevented such as in food industry. In addition, most of the liquid lubricants are environmentally harmful as the European Union has been placing some restrictions on use of these materials [4]. The liquid lubricants such as oils could also be evaporated in elevated temperatures, resulting in damage to surfaces.
The tribofilms generated by these lubricants can maintain a steady thickness which remains unaffected by a load, temperature and the like. In solid lubricating, tribological contacts lead to a transferring a thin layer of material from the surface of the coating to the counterface, usually known as a transfer film or tribofilm. Due to chemical reactions with the surrounding environment, the wear surfaces can show different chemistry, microstructure, and crystallographic texture from those of the bulk coating; so, these coatings illustrate different characteristics in different environments. For example, a typical solid lubricant can give extremely low friction and long wear life in one environment and fail in a different environment [4].

Diamond-like carbons (DLCs), transition metal dichalcogenides (TMDs), polymeric composite coatings and the like are among the solid lubricants which are commonly utilized. Usage of some surface and subsurface analytical techniques such as X-ray photoelectron spectroscopy (XPS), scanning electron microscopy (SEM), atomic force microscopy (AFM) and so on has provided the fundamental understanding of synthesis-structure tribology relationships in solid lubricant materials [5,6].

The present research work is aimed at investigating the effect of laser structural patterning on the tribological performance of W-S-C coatings.

Alloying TMD coatings with C or other elements enhances the mechanical properties and in case of well oriented TMD layer, formed in the contact, the coating could have a self-lubricating characteristic. This well-oriented coating would be easily formed if contact conditions including temperature, load and sliding distance are suitable enough to promote structural transformations. The formation of this layer in many applications such as plastics moulding, rubber contact and so on is not possible due to contact conditions.

In case of pure WS2, the well-oriented layer can work under soft conditions but it is not wear resistant. In fact, the ideal would be having the coating with good mechanical properties with the zones already transformed. Thus, alloying coating with C can provide a mechanical-resistant coating, transformed zones would give the better tribological properties. Recently, researchers have been trying to treat the structure of TMD coatings using laser irradiation with the aim of modifications towards the increase of purity and crystallinity of these coatings [7,8]. In fact, treatment of the coating could enhance the crystallinity and orientation of the TMD phase and therefore its lubricating properties. Due to significant advantages of the laser treatment such as ease of control of various parameters and efficiency, it is predicted that this process could improve self-lubricating properties in TMDs.

1-1-Framework

The research work titled “Influence of laser structural patterning on the tribological performance of C-alloy TMD coatings” is submitted in partial fulfilment of the requirements for the degree of Joint European Master in Tribology of Surfaces and Interfaces (TRIBOS). This is a preliminary study into the effect of laser treatment on structure of W-S-C coatings, carried out at the Centre for Mechanical Engineering, Materials and Processes (CEMMPRE) at University of Coimbra.

1-2-Aim and objectives

The main goal is to understand the structural change of W-S-C coatings, caused by the laser treatment and its effect on tribological properties. In addition, specific objectives will be directed towards the following work-plan;

A- Investigating the structural changes of treated W-S-C coatings using Raman spectroscopy

B- The characterization and the analysis of the treated samples using X-ray diffraction (XRD)

C- The evolution of friction coefficient of samples with sliding time using SRV machine

D- Measuring wear rate resulted from ball on disk test using the 3D profilometry

E- Investigating the structural changes of treated W-S-C coatings after sliding using Raman spectroscopy

1-3-Scope and thesis organization

The present thesis will be arranged and summarized in five chapters as follows:

The Chapter 1 is an introductive chapter where a brief survey on self-lubricating are given and the aims and objectives are drawn as well as the work plan.

The Chapter 2 provides a detailed background into TMD materials, state of the art, past, recently reviewed literature and published papers, properties, lubricating mechanism, fabrication and treatment processes.

The Chapter 3 will be allocated on sample preparation and treatment and identifying conditions of laser irradiation. In addition, the condition of characteristic techniques will be presented.

Chapter 4 will be focused on the analysis of the obtained results using different techniques including SEM (morphology), XRD (crystallinity), Raman (composition), Wavelength-dispersive spectroscopy (WDS) (the surface composition), ball-on-disk test (tribological properties) and indentation (mechanical properties).

In Chapter 5, all results and achievements will be concluded.

Chapter 2

2-State of the art

In this section, an overview about transition metal dichalcogenides (TMDs), their properties, fabrication and treatment processes are discussed. The most relevant works are summarized in what regards the most important topics of the present thesis.

2-1-Transition metal dichalcogenides

Transition metal dichalcogenides (TMD) have attracted a lot of attractions in different fields such as optics, electronics, and optoelectronics due to their distinguishing chemical and physical properties [9]. Employing TMDs in fabrication of various devices like gas sensors, energy storages, piezoelectric devices and the like is the best evidence for their outstanding capacities in different applications [10]. These materials also could be utilized to reduce friction in form of either an oil additive or a coating. [11]

MoS_2, WS_2, $MoSe_2$ and WSe_2 are examples of TMD compounds [9,12]. Tungsten Disulphide (WS_2) is a chemically inert material which can bond with substrates to form a thin film. It is ALSO, used in plastic moulds and extrusion dies to release materials from moulds [13].

2-1-1-Structure

TMDs are considered as layered materials which have a strong bonding within the layer and weak Van der Waals interaction between the layers. TMDs are known with a general formula MX_2, where M stands for a transition metal from group IV (Ti, Zr or Hf), group V (V, Nb or Ta) or group VI (Mo, W), and X represents a chalcogen atom such as S, Se or Te [14, 15]. The Figure 1(left) illustrates the schematic structure of atomic layers of TMDs. In this structure, every layer of metal atom is sandwiched between two sheets of chalcogen atoms. In such a structure, metal atoms are six-fold coordinated within a triple layer and their bonding geometry includes either trigonal prismatic or octahedral arrangement. As shown in the Figure 1(right), in the trigonal prismatic configuration the two chalcogenide planes place directly above each other, whilst in octahedral one they have 180-degree difference. The Figure 2 illustrates three polymorphs for TMDs including 1T, 2H and 3R. The numbers show the number of layers in the unit cell and the letters stand for symmetry, namely T-trigonal, H-hexagonal, and R-rhombohedral. The c axis perpendicular to the layers, the a and b axis along the minimal chalcogen-chalcogen distance can be used to define the unit cell. The hexagonal form is popular in friction reduction applications. This low friction property of hexagonal TMDs comes from their lamellar crystal structures [16].

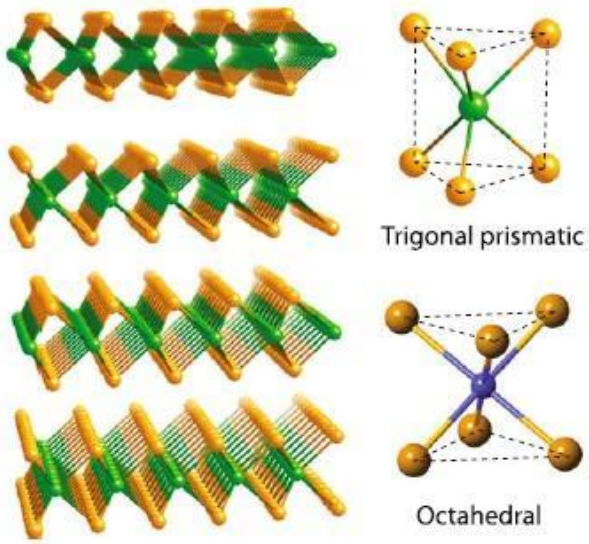

Figure 1. The three-dimensional schematic structure of an atomic layered TMD (left), and the trigonal prismatic and octahedral arrangements (right) [16].

In fact, materials with sandwiched structures can be utilized to reduce friction, but they are not as efficient as a hexagonal form of TMDs. In addition, the adhesion between DMT coatings and the substrate is greater than adhesive forces between lamellae; so, the lamellae readily slip related to each other, resulting in a very low friction coefficient [11].

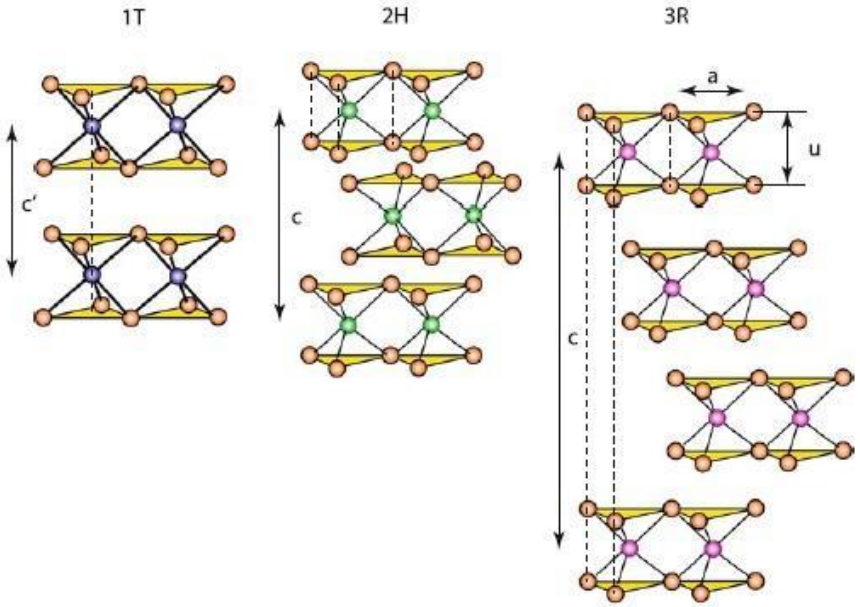

Figure 2. Schematics of the structural polytypes of TMDs [11].

Another advantage of TMDs lubrication in comparison with other layered materials such as graphite is that in case of graphite lubrication, some intercalating species like

H_2O are needed to achieve low friction condition; whist the TMDs are intrinsic and even perform better in the absence of such contaminations [17].

As a plane parallelly in contact with TMD layers starts to slide, the Van der Waals weak bonds between layers are readily broken, leading to low friction sliding; while the strong bonds between chalcogen and the metal atoms remain without any damage. It is worth noticing that if crystalline planes are perpendicular to the sliding surface, the self-lubrication would not take place. Under the sliding condition, the layers are moved or rotated to reorient and become parallel to the substrate. In fact, due to the alignment of basal planes, the coating would adopt itself to the new tribological contact condition, resulting in the formation of an easily sheared tribolayer [11, 17,18].

The vacuum condition, not only could result in the very low friction coefficient of TMDs, but also, the ultra-high vacuum would lead to super lubricity in which resistance to sliding nearly vanishes [19].

The vulnerability to oxidation is one of TMDs' drawbacks, particularly when they are not in an appropriate orientation, which results in more reactive crystal edges [20]. Additionally, this would promote porosity and subsequently penetration of contaminants like water and oxygen [21]. Such species can readily react with dangling bonds, present at the end of the crystallites and disturb the sliding of layers over each other and their reorientation in the contact area, and generally reduce lubrication properties [18,21].

2-1-2-Properties

2-1-2-1-Tribological properties

The TMD coatings can present adaptive behaviour by creating tribolayers. Interestingly, the rise in temperature and/or applied load could promote the growth of these tribolayers and as a result, declining the wear rate. However, the thermal and oxidation resistance would be restricted and wear rate tends to increase [22]. Due to their unique highly anisotropic crystal structure, these materials can be used as a solid lubricant with friction coefficient lower than 0.01 and acceptable hardness that creates transfer layers resulting in low wear rates. It should be mentioned that in case of mechanical applications, friction coefficient lower than 0.001 is not required and in many applications, even two orders of magnitude higher friction would be acceptable [11].

There are three basics to have tribological properties in TMD coatings; first of all, there should be no contaminant either in the TMD coating or in a surrounding environment. For example, water could considerably disturb easy sliding of basal plates. Secondly, the adhesion forces between the coating and the substrate should be greater than those of between lamellae themselves, resulting in preferential slipping between the lamellae and lowering the friction. Under such condition, TMD transfer layer is progressively

formed on the counterpart. Thirdly, the friction and resulting shear stress would cause the reorientation of the basal planes in the tribolayer and the film itself [23].

2-1-2-2-Hardness

In comparison with other types of low friction coatings such as diamond-like carbon (DLC), the TMDs have lower hardness and depending on some factors such as stoichiometry, morphology, and deposition conditions, the hardness value ranges from 0.3 to 2 GPa [24]. Using some techniques like doping with a third material such as carbon, nitrogen and so on, the hardness of TMDs could be increased considerably [25].

2-1-2-3-Adhesion

The TMD coatings have very low adhesion to the substrate, making them inefficient for tribological applications. Using an interlayer is a useful solution to promote adhesion between the coating and the substrate. For instance, an optimized Ti interlayer could increase the scratch test critical load from 5 N up to 25 N for a specific W-S-N film [26].

There are several factors, promoting the good adhesion including reducing local stress levels, strengthening the atom-atom bonding in interfaces, using a material with high fracture toughness, the absence of easy deformation or fracture modes.

Conversely, using brittle materials, having poor interfacial bonding and so on would lead to a reduction of adhesion [27, 28].

2-1-3-The lubricating mechanism

As mentioned earlier, the weak Van der Waal's forces between the lamellae of TMD basal planes result in intra- and inter-crystalline slip in friction contact and therefore, diminishing the tangential force necessary for the sliding [29]. In fact, applying a shear force causes the basal planes to slide over one another, resulted from an inter-crystalline slip and transfer to the rubbing counterface [30]. The mechanism of the lubricity of a layered material involves inter-film sliding, intrafilm flow and film/substrate or interface slip. Indeed, in case of lamellar solid lubricants, lubrication is provided by an interlayer shear mechanism; because the crystal structures of these materials consists of atoms lying on the same layer which are closely packed and strongly bonded to each other, and the layers are relatively far apart and the forces that bond them (e.g., Van der Waals) are weak. This mechanism is schematically illustrated in the Figure 3[31].

In the other word, within the structure of a TMD coating, the layers are quite flexible and they can slide over each other without any damage and under repeated sliding, layers can move considerable distances over the substrate. This relatively free movement of adjacent layers is the lubrication mechanism of TMDs [32].

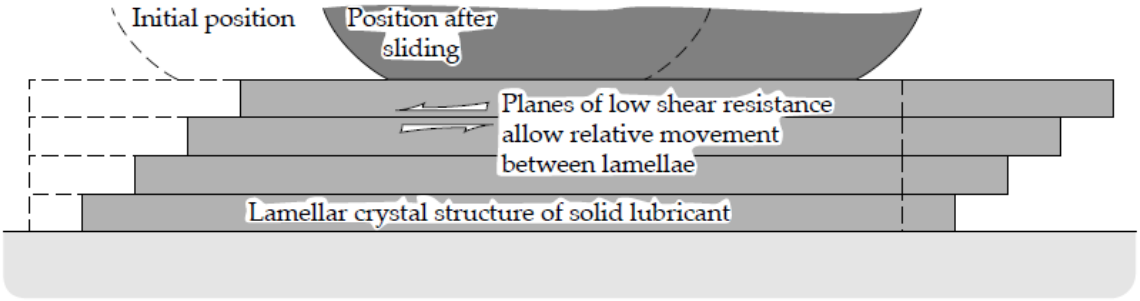

Figure 3. Mechanism of lubrication by a TMD coating [31].

Due to strong interatomic bonding and packing in each layer, TMDs are very high in-plane strength which increases wear life and reduce wear damages. During sliding, crystalline layers of these solids align themselves parallelly to the direction of relative motion and slide over one another easily to provide lubrication. In addition, the formation of a smooth transfer film on the sliding surfaces is very important for long wear life and dissipation of frictional energy [32].

2-2-Physical vapor deposition (PVD)

Physical vapor deposition (PVD) is a coating technique in which the coating material is applied on the substrate from a vapor phase to create a thin film. Both metals and non-metals can be deposited using this process. Indeed, PVD is employed to deposit a thin film of various types of materials including elements, alloys and compounds [33, 34, 35]. In this process, the raw material is heated and evaporated from the target using a high energy electron beam or thermally heated filament. Vacuum, low-pressure gas and plasma can promote transferring the vapored material to the substrate where it is condensed [33].

Generally, there are two PVD groups for fabricating coatings in vacuum conditions, namely evaporation and sputtering techniques. The next section is devoted to DC magnetron sputtering technique which has been used to prepare the thin films in this work.

2-2-1-Sputtering technique

Sputtering is a deposition process in which the ejecting atoms from targets using high energy ion bombardment are deposited and condensed on the substrate to form atomic film later [33,34,35]. This technique is performed using plasma or glow discharge generated by either direct current (DC) or radio frequency (RF) power which is used to sputter electrically conductive materials and electrically insulating materials, respectively [36]. In addition, thin films like oxides and nitrides can be deposited with very low deposition rate by reacting the metal with a gaseous phase such as oxygen and nitrogen. The magnetron-type discharge technique is suitable to achieve higher deposition rates [33,37,38]. To increase the deposition rate, the gas pressure should be

dropped in the chamber which leads to a longer mean free path for an atom-gas collision during transferring from the target into the substrate. Under the high pressures, the number of collision increases resulting in decreasing in the deposition rates. On the other hand, the low pressures also are needed to control the amount of contamination in the chamber and also maintain high ion energies [33,37,39].

2-2-1-1-Magnetron sputtering

Magnetron sputtering is important in both industrial applications and science and technology research. Using this technique, many experiences in deposition of different kinds of materials such as metals, alloys, intermetallic compounds and so on with a wide range of application have been achieved [40]. This technique is considered as a complementary method related to other vacuum coating techniques such as thermal evaporation and electron beam evaporation by overcoming some problems associated with these techniques like low deposition rates, low ionization efficiency in the plasma, and high substrate heating effects [38].

There are several primary advantages in the use of magnetron sputtering technique including high deposition rate, ease of sputtering any metal, alloy or compound, high purity films, extremely high adhesion of films, excellent coverage, excellent uniformity on large areas and the like [37].

In this process, a magnetic field which is parallel to the target limits secondary electron motion to the vicinity of the target. As seen in the Figure 4, one of magnet's pole is placed at the central axis of the target and another one is formed by a ring of magnets around the outer edge of the target [38].

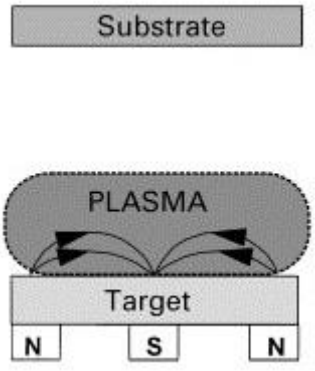

Figure 4. A schematic representation of the magnetron sputtering system [38].

In fact, the magnetic field forces the electrons to circulate in a path around the target and traps them in the vicinity of targets. Thus, electrons will have longer travelling paths and the probability of interaction between them and the present gas (usually Ar) is raised and increased ionization of the gas occurs, resulting in increase in plasma density and consequently the deposition rate [3838].

Despite all advantages, the magnetron sputtering has an inherent disadvantage which is the non-homogeneous ion current distribution across the target surface caused by the trapping of electrons in the magnetic field [41].

2-3-Alloyed TMDs

The columnar and porous structures of TMDs are prone of many failures and they need to enhance adhesion and provide some levels of protection against contamination. Introducing some materials such as N and C, into these structures can prevent the formation of the large-size grains in the film and stops columnar growth, typically resulting in an amorphous structure. Doping can lead to having a denser structure and consequently improving the film's hardness [26, 42]. Studies on C- or N-alloyed tungsten disulphide (WS_2) have confirmed the rising in hardness and modifying the mechanical properties of WS_2 which reached their peak at dopant content near to 50 at.%. For example, alloying W-S films with carbon increased significantly the hardness in the range of 4–10 GPa [23,43,44]. In addition, it is worth noticing that formation of such an amorphous structure does not necessarily result in lower friction coefficients.

2-4-Treatment

A coating needs to meet some certain criteria to be considered as a good solid lubricant. First of all, there should be an enough shear strength of adhesion between the lubricant layer and the substrate to maintain a desired boundary lubrication. Secondly, the internal cohesion of the coating has to good enough to prevent disintegration of the coating during sliding. In addition, to reduce the resistance against friction, the adhesion between the particles and the layers in the shearing direction must be as small as possible [45]. If each one of these requirements is not fulfilled by the coating, some treatments could be utilized to improve the quality of the system.

As seen before, there are many methods for producing thin films, such as vapor deposition method. To enhance the desired properties of the deposited films, various surface treatment techniques have been developed [46]. Laser treatment is one of the surface treatment techniques which facilitates the controlling various parameters in a very efficient way [47].

2-4-1-Fundamentals of laser processing

During laser processing, energy would transfer from the laser source to the exposed material. In fact, laser is a form of light, which has both particle and wavelike behaviours. In the other word, it can interfere with matter like a particle and diffract like a wave. Based on Max Planck's law, there is an inverse relationship between the energy and the particular wavelength. Absorption has a significant role to play in photon-photon energy transfer and the higher absorption results in higher energy absorbed by the material. In addition, the wavelength of the light is very important in getting enough energy for absorption by the desired material. Figure 5 illustrates different types of light along with their wavelengths. According to this figure, the light

with a longer wavelength like infrared radiation has less energy than those of with a shorter wavelength such as UV [48].

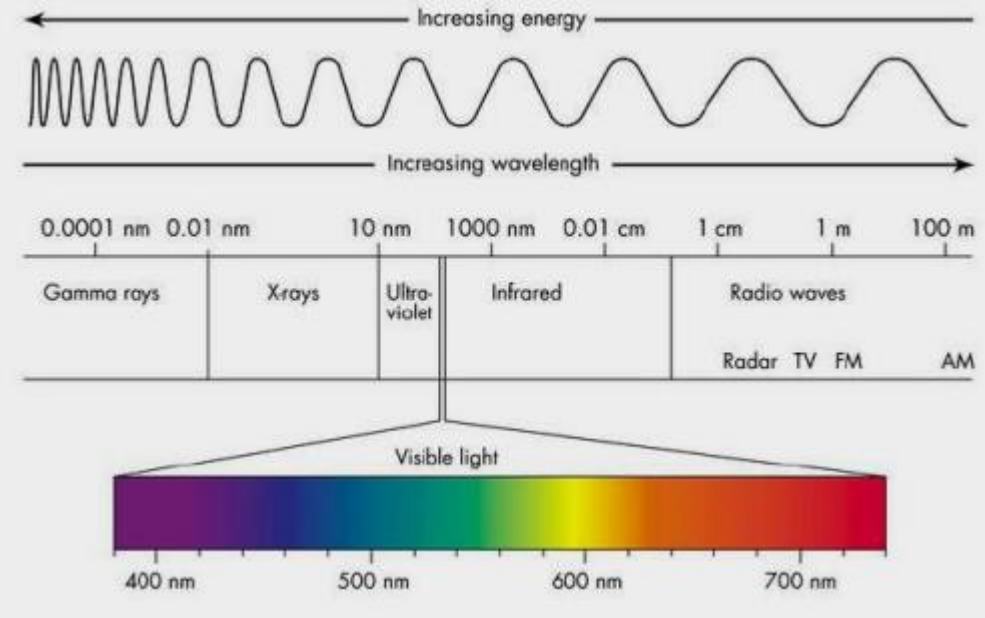

Figure 5. Spectrum of light and energy [49].

In case of laser, there are several technical parameters which can affect the resultant material properties including applied power density distribution on the exposed surface, interaction time, scanning velocity of beam and pulse width.

Power density can be defined by combination of laser power and spot size, used to state how much energy and heat are delivered to the surface; so, one can increase output power by controlling density. For instance, to deliver desired energy, an available option is to alter the spot size to create a suitable power density [48, 50].

The beam size of a laser beam with a Gaussian distribution is defined as the radial distance at which intensity of the beam declines to $1/e^2$ or 13.5% of the beam energy [51].

Pulse width is used to explain the delivery time or exposure time of the selected energy reaching to the surface. It is clear that different target values need different exposure time. Thermal relaxation time (TRT) plays an important role to understand pulse width. This component is the unit time for a target to release more than half of the gained temperature [50].

As laser beam is focused on the surface, it creates deeper impact at a narrow diameter. While it is defocused, penetration depth is more superficial but exposed area on the surface is wider. As seen in Figure 6, to defocus the beam, the distance between the lens and substrate should be increased form d_1 to d_2 ($d_1 < d_2$) [52].

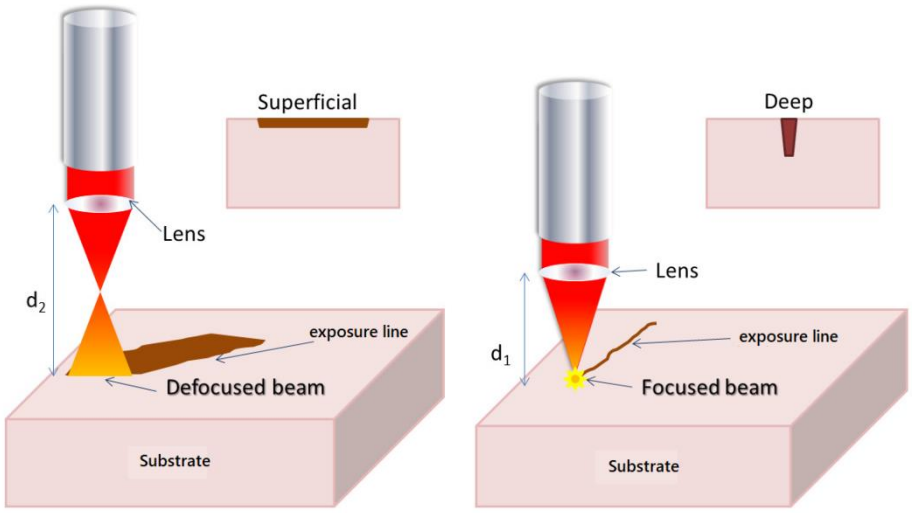

Figure 6. The focusing and defocusing process of laser beam [52].

This ability of laser can be used in many applications such as the surface treatment at various spot sizes with different penetration depth.

2-4-2-Advantages of laser surface treatment (LST)

There are several advantages in employing laser radiation for the surface treatment. First of all, due to ease of handling this form of energy, the treated area can be readily controlled in depth, extent and time above temperature. Secondly, the surface treatment by laser is chemically clean and there is no need to touch the surface. Because of the lack of environmental disturbance during the process, automation is usually possible; so, the process could be controlled by computer [53]. Laser technique has been used to fabricate a good solid lubricant layer from mixture of graphite and boron nitride. In fact, using this technique has resulted in reducing in friction coefficient of the samples [54]. The laser irradiation can be used to treat non-hydrogenated DLC coatings that during treatment the modified region expends and causes radial compressive stress and tangential tensile stress [47].

The laser beam not only can generate high heat load on the surface, but also causes instantaneous pressure built upon it, due to very short duration of the laser beam. Both factors, namely high heat load and instantaneous pressure, build up by laser beam on the layered materials such as graphite can cause surface change as well as crystallographic transformation. For example, in case amorphous graphite, it gets transformed to crystalline structure after laser irradiation [55].

The researchers have been shown that MoS_x-based single and few-layered materials have a good visible light absorption and versatile chemistry including various compositional and structural transformations due to laser treatment. The Raman spectroscopy can be employed to characterize different TMD polymorphs including T, H and the like [56].

2-4-3-Classification of laser surface treatment processes

Generally, there are four main categories for laser surface treatment processes, namely laser surface heating, laser surface melting, laser surface shocking and laser ablation [57].

2-4-3-1-Surface heating

Laser surface heating is a suitable replacement for localized heat treatment technologies like flame or induction hardening. During this process, the temperature distribution never exceeds the melting point of material and due to short interaction time, the homogeneity of treated layer is affected by prior microstructure of the layer. The finer microstructure can be treated more homogeneously. In this category, laser transformation hardening is considered as a new processing technique for treatment used for improving of hardness and strength of materials.

2-4-3-2-Laser melting

In laser melting, the temperature of the exposed area exceeds its melting point and followed by a rapid quenching procedure to obtain better properties as a result of rapid solidification. This process is utilized to improve surface hardness, refined structure, corrosion and wear resistant properties of cast iron, tool steels, stainless steels, titanium and aluminium alloys [57].

2-4-3-3-Shock hardening

To generate a shock wave, the laser beam should be applied in a very short interaction time with a very high-power density; as high stress of the shock wave results in developing significant plastic strain in the surface and consequently improving in physical and mechanical properties. In addition, a pulsed laser beam can be employed to selectively remove the surface of a material, using high power densities in a short interaction time [57].

2-4-3-4-Laser ablation

The laser ablation is a method to remove material using directing a focused beam with minimal size around 25 microns in diameter. Using this process, it is possible to have highly tailored removal, so parts or sections of the surface can be removed as needed. In addition, since the laser energy can be selectively absorbed by materials, so this technique is utilized for cleaning surface, removing previous coatings to prepare surfaces for applying new coatings without any damage to substrates.

Furthermore, laser ablation has other applications specially as a deposition technique. In this application, the coating material is ablated from a target using laser beam and deposited on the surface as a coating. This deposition process is a subcategory of physical vapor deposition known as pulsed laser deposition (PLD) and it can be employed to deposit materials which are not easily evaporated by conventional techniques [53, 58, 59].

2-4-4-Laser types

There are many types of lasers used in researches, industry, and the like. Lasers are often described by the kind of lasing medium they use including solid state, gas, excimer, dye, or semiconductor. In this work, two types of common lasers namely UV laser and neodymium-doped yttrium aluminium garnet (Nd:YAG) laser will be utilized.

2-4-4-1-UV lasers

Nowadays, using UV lasers as a source of ultraviolet light is common due to two main reasons; firstly, UV laser can provide a sufficiently powerful energy flux and secondly the properties of the UV light are ideally suited to many applications such as in microstructuring with a high-resolution beam.

There are a lot of advantages to using UV lasers as opposed to infrared or visible lasers. Employing infrared or visible lasers can melt or vaporize material that can prevent the formation of small features and consequently damage the structural integrity of the substrate; while, during UV lasers process, the atomic bonds in the substrate are directly broken, resulting in no peripheral heating generating around the beam spot. So, this declines damage to material and allows UV lasers to process thin and delicate material much more efficiently than visible and infrared lasers. Even it facilitates the creation of very precise cuts, holes, and other fine features. Since, laser spot size is directly proportional to wavelength; so, UV lasers have a higher spatial resolution than visible or infrared lasers, leading to more precise processing of materials [60].

2-4-4-2-Nd: YAG lasers

This type of laser is generated from crystalline YAG with the chemical formula $Y_3AL_5O_{12}$ which has a wavelength of 1.06μm. Due to its shorter wavelength, temperatures and nature of the surface, higher absorption for metallic materials happens. The advantage of Nd:YAG laser over other type of lasers such as CO_2 laser is that because of its shorter wavelength and its ability to deliver laser radiation through optical fibres, the pulse Nd:YAG laser has variety of applications in various forms of material processing including alloying, cladding, drilling, spot welding, and laser marking than other type of laser [61].

Chapter 3

3-Experimental part

The objective of this work was to study the effect of laser structural patterning on the mechanical and tribological performance of carbon-alloyed WS_2 coatings. The samples were prepared by DC magnetron sputtering procedure to achieve W-S-C coatings with approximately 50 at. % C content. The different types of patterns were employed to treat the samples using two different lasers, namely UV and YAG lasers. The treated samples were characterized concerning their structure, mechanical and tribological properties using techniques like optical microscopy, Raman microscopy, XRD, nanoindentation and tribometry.

3-1-Deposition procedure

The W-S-C coatings were deposited in a vacuum chamber from C, WS_2 and Cr targets using UDP 650/4 Teer Coatings deposition equipment (Teer Coating Limited). Before the process, the M2 steel substrates were polished with 400, 600, 1000, 1200 sand papers, following with diamond pastes with particle sizes 3μm and 1μm in order to obtain smoother surfaces and coating adhesion. In addition, they were cleaned ultrasonically for 15 min, followed by drying using air before placing in the chamber. There were two graphite targets (99.99 %) and one WS_2 target (99.9%) to achieve the desirable chemical composition. The substrates were put in a rotating substrate holder and the chamber was vacuumed about 5×10^{-4} Pa. The targets and samples were cleaned in an argon atmosphere for 40min using pulsed-DC current (Advanced Energy Pinnacle Plus) at bias voltage of 600V.

The process was continued by deposition of the Cr interlayer for 10min with a thickness of ~400 nm, to promote the adhesion between the substrate and the main coating. This chromium interlayer (300-360 nm) was deposited on the substrates in order to improve adhesion between the top layer and the steel substrate. Afterwards, the gradient layer was deposited for another 10min by decreasing the voltage on Cr target and increasing the voltage on WS_2 and C targets. To achieve C contents around 50 at. % the power density employed for each graphite target was set to 2.6 and 3.2 W/cm_2. The whole sputtering process lasted about 2 hours.

3-2-Treatment procedure

The laser used to treat these test samples was a Nd:YAG (1064 nm wavelength), model Starmark SMP from Rofin, operated in the pulsing mode. This laser allows using a wide range of parameters such as scan speed (20-2000 mm/s), laser irradiation power (3.5-25 W), pulse frequency (4-30 kHz), distance between lines and so on. The distance between lines was set to 100 μm and only a single pulse per interaction was used. In addition, the sample position (relative to the laser focus) seemed to have a significant

impact on reducing laser ablation at the sample surface. After all, gentler laser thermal pulses were delivered to the sample i.e. higher scanning speeds, lower frequencies and lower laser powers, and laser defocus, were found to result in the desired phase transformation.

In addition, a suitable mask was designed with a UV laser by machining a copper foil with the same dimensions of the host round sample, with only a quarter of circle filled with a grid of several 100 µm diameter spots. This mask was then used to cover the sample prior laser irradiation, where the grid area is placed over the sample quadrant aimed to be laser irradiated.

According to the above details, the different sample were irradiated based on conditions listed in Table 1.

Table 1. The conditions of the YAG laser irradiation in each sample as well as the reference sample.

Sample	Condition	Position (below the laser focus)	Laser power (W)	Scan speed (mm/s)	Pulsing frequency (kHz)
YAG 1	Without mask	30mm	4.5	2000	4
YAG 2	With mask	30mm	4.5	2000	4
YAG 3	With mask	25mm	4.5	2000	4
Reference	-	-	-	-	-

There were four samples treated by the UV laser which is a pulsed UV (355 nm) Inngu Laser with maximum power of 3W. The laser is fitted with a scan head with a F-theta lens (160 mm focal distance, 100×100 mm^2 max. scanned area). The first pattern includes a uniform square grid of dots (pulse centre) separated by 20 µm. The dots were patterned at 100 mm/s and 75 kHz pulses with Q-switch duration of 10 µs. The second hatched sample includes a set of lines separated by 10 µm, prepared at the 1000 mm/s speed and 75 kHz pulses with Q-switch duration of 10 µs.

Table 2. The conditions of the UV laser irradiation in each sample**.**

Sample	Pattern	Distance	Laser power (mW)	Scan speed (mm/s)	Pulsing frequency (kHz)
UV 1	Dots	10µm	4	100	75
UV 2	Compact dots	-	30	1000	75
UV 3	Parallel lines	10 µm	25	500	75
UV 4	Grid	10 µm	25	500	75

The third sample, treated by the UV laser consists of the parallel lines which were patterned at 500 mm/s speed and 150 kHz pulses with Q-switch duration of 4.6 µs. the last pattern consists of intersecting lines, and the treatment conditions are similar to previous sample. The characteristics of UV treated samples illustrate in Table 2.

3-3-Characterisation techniques

3-3-1-Raman spectroscopy

Raman spectroscopy is widely employed to provide a structural fingerprint for molecules identification. The microstructural changes, impurities, residual stress, and the like are among the factors which can affect the Raman vibration spectra of materials. These factors can appear as Raman information, namely, band position, band position shift, full width at half maximum (FWHM), and intensity [62].

Raman spectroscopy can be used, as an efficient method, for the chemical identification and the structural analysis of WS2 and carbon.

All samples were characterized by micro-Raman analysis, conducted in the backscattering configuration on a Horiba HR800 instrument using a 600 lines mm^{-1} grating and the 441.6 nm laser line from a HeCd laser (Kimmon IK Series, Japan).

A 100x objective (spot size ~ 2 mm, numeric aperture = 0.9, Olympus, Japan) was used to focus the laser light onto the sample and to collect the backscattered Raman radiation to be detected by a Peltier cooled (223 K) CCD sensor. Acquisition time was set to 1minute.

3-3-2-Optical microscopy and Scanning Electron Microscopy (SEM)

The optical microscopic investigation of treated and untreated samples was preformed using ZEISS Axio Imager Z2m equipment. Different objective lenses were employed to take the images. This technique was helpful for initial investigation of samples, their patterns and some estimations. Cross-sectional micrograph of the coating in its as-deposited state was taken using a field emission SEM (Zeiss Merlon). An analysis of the chemical composition was performed using WDS equipment mounted on the SEM.

3-3-3-X-ray diffraction (XRD)

X-ray diffraction (XRD) is a widespread used technique for structural characterization. As a high-tech, non-destructive tool, XRD can be employed to analyse a wide range of materials including fluids, metals, minerals, polymers, catalysts, thin film coatings and ceramics. In this equipment, the monochromatic X-rays are generated by a cathode ray tube, then filtered to produce monochromatic radiation, collimated to concentrate, and directed toward the sample [63].

The characterization and the analysis of the samples were performed by Philips X-Pert Pro MPD diffractometer using Cu Ka radiation (λ = 0.154 nm) in conventional (θ-2θ)

mode. The equipment was adjusted to start angle from 5 degrees and end up at 75 degrees. The scan step size was 0.02500 degree with 2 seconds per step. The total acquisition time was about 1.5 hour. The XRD measurements were performed at a 40kV voltage and 35mA tube current. In addition, a grazing incidence angle of 2^o was used to carry out the grazing incidence x-ray diffraction (GIXRD); because during scanning a thin film by conventional θ - 2θ, the beam penetrates deeper thickness that results in producing weak signals from the coating and intensive signal from the substrate. So, to minimize this effect it is suggested to use the X-ray diffraction at the grazing incidence (GI-XRD). In this mode, a small and constant incident angle (1^o-3^o) would be employed which leads to scattering at small depth [64].

3-3-4-Nanoindentation

Nanoindentation is a common technique to measure the mechanical properties in small scale. Using this tool, indentation to very shallow depth would be possible, so that minimal influence from substrate is obtained. There are several components in a nanoindentation test, namely sensors and actuators, used to apply and measure the mechanical load and indenter displacement as well as the indenter tip. During the test, the indenter is pressed into the surface with a prescribed loading and unloading profile, and force and displacement are recorded as load-displacement curve [65, 66].
Hardness, H, is the resistance of the material against plastic deformation due to indentation which could be calculated by following equation.

$$H = \frac{F_{max}}{A_C}$$

where F_{max} is the maximum applied load, and Ac is the contact area of the indentation immediately before unloading. Once the load is applied to the indenter, the depth of indentation on the sample is measured. The geometry of the indenter plays an important role in determination of the size of the area [67, 27].
The NanoTech Nanointerder (Micro-Materials Ltd.) Nanoindentation equipment was employed to measure hardness and Young modulus of the samples using a Berkovich diamond pyramid indenter.
The hardness and modulus of the samples were measured in the average of 20 different spots at the ambient temperature(23^oC). To measure hardness, a maximum 3.07mN was applied. The nanoindentation load vs/ displacement curves are presented in Appendix
The indentation depth is 10 % of the coating thickness of W-S coating.

3-3-5-Tribological properties

The alloying WS_2 with carbon presents a coating combining small hard WC and lubricant WS2 nanograins embedded in an amorphous carbon matrix. The main goal of this concept is to combine the excellent tribological properties of DLC coatings and the extremely low friction of the WS_2 phase [42].
To investigate the tribological properties, the measurement of fiction coefficient and wear rate could be employed. The wear rate is usually calculated using the so-called

Holm or Archard wear relationship which is a practical for the amount of wear. According to this equation, the wear coefficient or specific wear rate, K, is

$$K = \frac{V}{w.s}$$

where V is the worn volume, w is the normal load, s is the distance moved [68].

The equipment used in this work was an SRV machine which allows the steel balls oscillate under normal load against a stationary lower test sample. The load was adjected on 5N for a 10min duration. The frequency was 25Hrz with a stroke length of 2mm, resulting in an average sliding speed of 0.1 m/s. To determine wear rate of samples, their 3D surface profiles were obtained using the Bruker Alicona InfiniteFocus 3D profilometer, and then the profile across the wear track were measured to calculate the sectional area. Afterwards, the average of three sectional-area measurements from left, middle and right of scarred area was multiplied by the length of the scar to calculate the volume of the material removed during sliding. By putting this value in Archard equation, the wear rate of the sample would be obtained.

Chapter 4

4-Results and discussion

This work is aimed at studying the effect of laser structural patterning on the tribological performance of W-S-C coatings. In fact, the goal is to develop an understanding of the structural change of the coating due to laser treatment and its influence on mechanical and tribological properties.

Table 3 illustrates the elemental chemical composition of the W-S-C coating determined by WDS analysis. Furthermore, according to the scanning electron micrograph of fractured cross section shown in Figure 7, the total thickness of the coating is about 1.5µm and there is no a columnar structure (like those exist in common undoped W-S films) in the coating. This could be predicted an amorphous structure, which would be confirmed later using XRD.

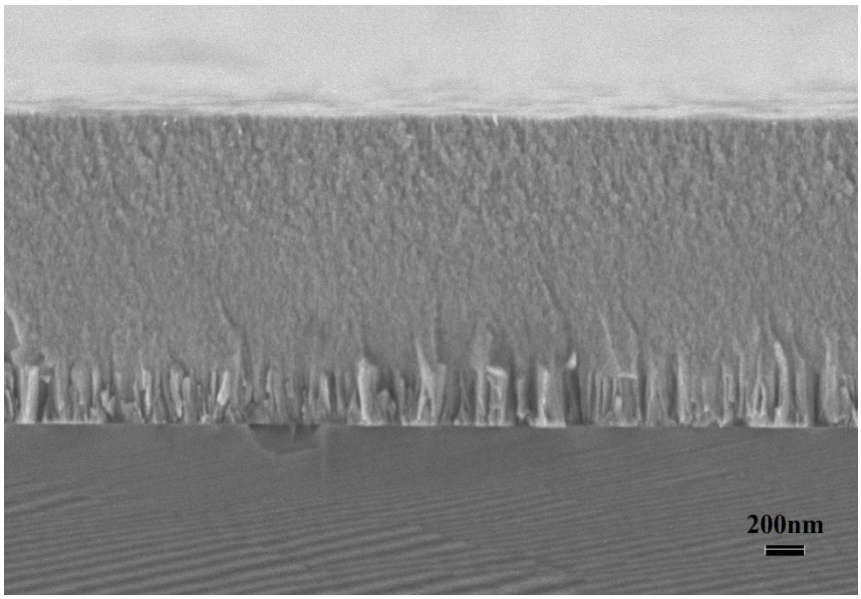

Figure 7. The cross-sectional SEM micrographs of the W-S-C sputtered coating.

Table 3. Chemical composition and thickness of W-S-C coatings.

Coating	**Chemical composition (Atomic percentage)**						**Thickness**
	W	Cr	S	Si	O	C	**(µm)**
W-S-C	17.2	0.8	29.3	0.1	5.0	47.6	1.5

The samples were the WS coatings doped with 50% carbon and treated by two types of lasers, namely UV and YAG lasers. Seven different patterns have been used to prepare samples. Table 4 shows some details about the samples as well as approximately

affected areas which were estimated using data from the optical microscopy. Furthermore, Figure 8 presents the schemes of patterns used for the laser treatment.

Table 4. The characteristics of samples.

Laser type	sample	pattern	Affected area (~)
UV	UV 1	Arrays of spots	20%
	UV 2	Compact spots	>70%
	UV 3	Parallel lines	8%
	UV 4	Intersecting lines	25%
Nd:YAG	YAG 1	Random spots	
	YAG 2	Arrays of spots	17%
	YAG 3	Arrays of spots	17%

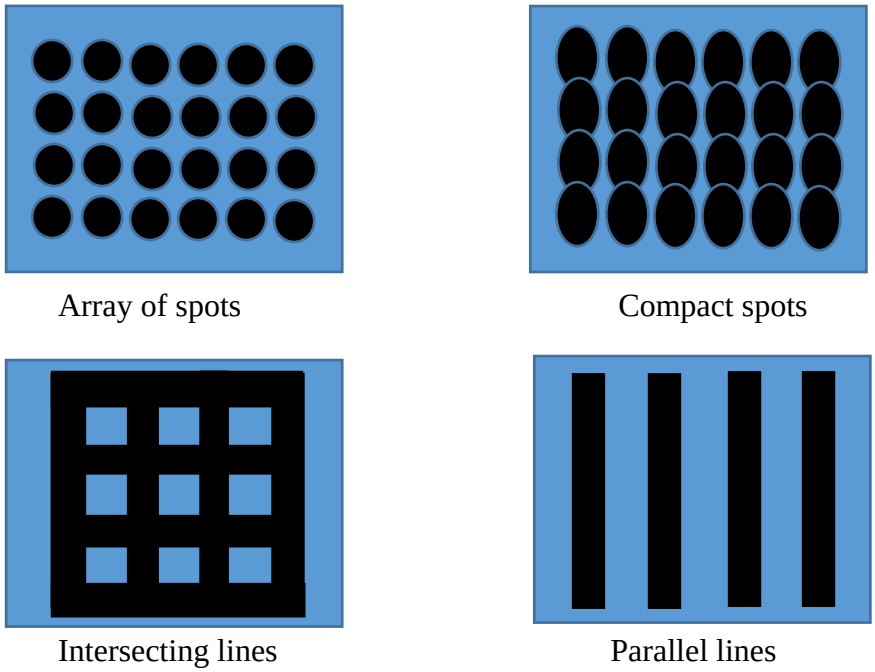

Figure 8. The schemes of patterns used for the laser treatment.

Using the optical microscopy, some primary investigations of the samples' surfaces were carried out. Figure 9 (left) presents the optical microscopic picture of untreated sample, taken using a 20X objective lenses. As seen in the Figure 9 (left), there are some dark spots on the untreated sample, which could be attributed to contamination. Figure 9 (right) also shows the morphology of the untreated sample, obtained by the field emission SEM which confirms its uniform surface.

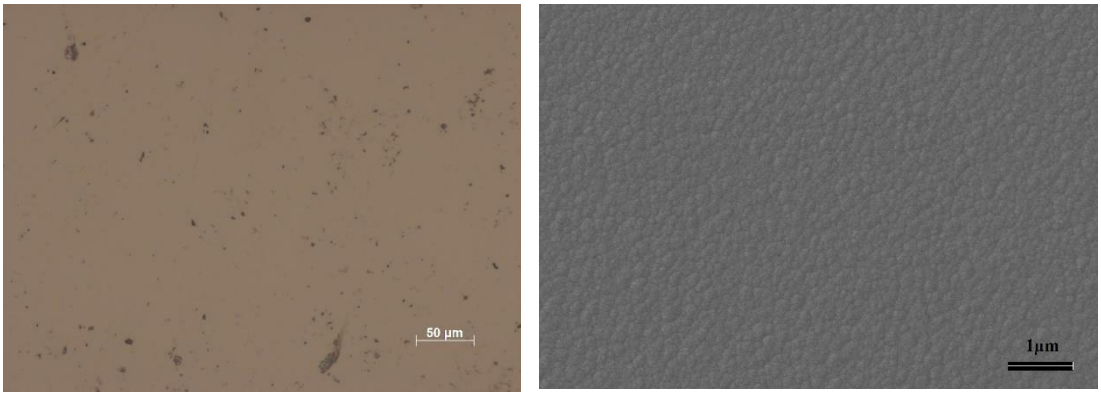

Figure 9. The optical micrograph (left) and surface morphology prepared by the field emission SEM (right) of untreated sample.

Figure 10 (a) to (d) illustrate optical microscopic pictures of UV 1, UV 2, UV 3 and UV 4, treated with the UV laser. As seen in the Figure 10(a), the spots are about 17µm in diameter and the distance between two arrays is about 40µm. Based on the calculation, the exposed area is about 20% of all. In addition, the central area of some spots is darker than other parts which could be due to over exposure and graphitization. As it is obvious in the Figure 10(b), the pattern consists of compact arrays of dots which in some areas, they overlap on each other. The colour of their boundaries is lighter than the dots and it seems exposure resulted in graphitized dots. The size of dots also is about 10µm and they are dark and uniform in colour. The exposed area consists of more than 70% of whole area.

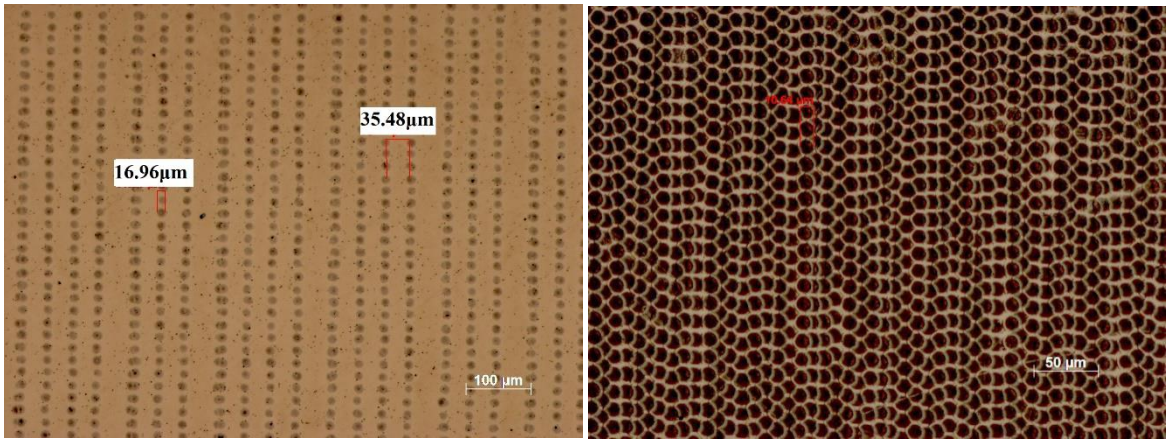

(a) (b)

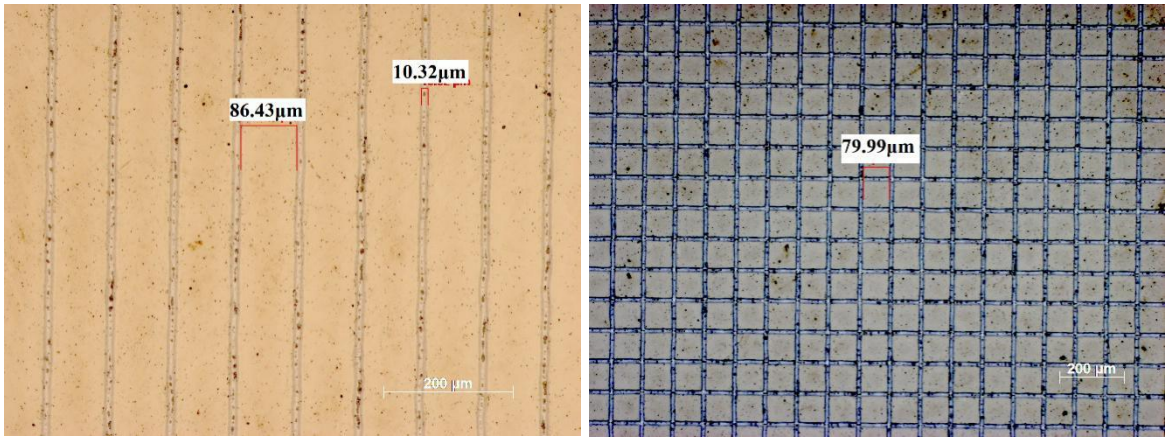

(c) (d)

Figure 10. The optical microscopic pictures of UV 1 (a), UV 2 (b), UV 3 (c) and UV 4 (d).

The UV 3 are treated by UV laser with a pattern consists of parallel lines (Figure 10(c)). The width and distance between them are about 10 and 90µm, respectively. About 8% of the whole area was treated by the laser. Same as UV 3, there are some dark spots in the radiated areas of UV 4 which could be attributed to graphitization of these areas (Figure 10(d)). The percentage of the radiated area in relation to all is about 25%.

Figure 11(a) to (c) illustrate optical microscopic pictures of samples treated by the Nd:YAG laser. As presented in Figure 11(a), YAG 1 was prepared without mask and the spots on its surface, are donut-shaped with diameter about 1µm. Figure 11(b) is attributed to YAG 2, treated using mask by Nd:YAG laser.

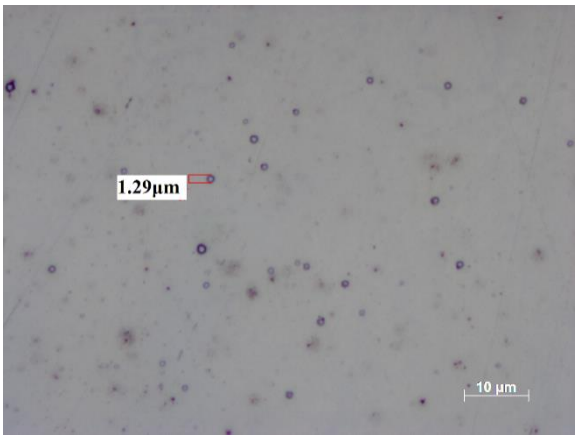

(a)

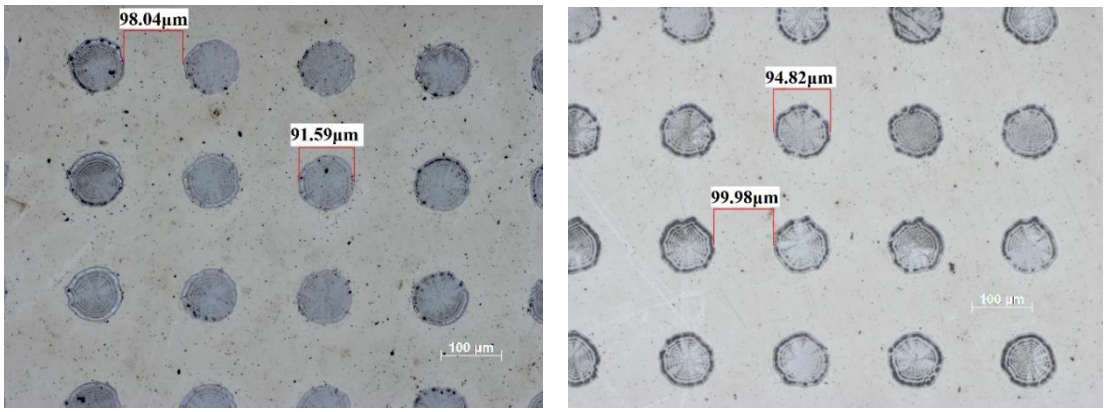

(b) (c)

Figure 11. The optical microscopic pictures of YAG 1 (a), YAG 2 (b) and YAG 3 (c).

As it could be seen in the picture, some spots are more or less uniform in colour and dark areas are less generated in the exposed area. The spots are almost circular in shape with about 90µm diameter. The exposed area includes approximately 17% of total area. The Figure 11(c) is related to YAG 3 which was treated by Nd:YAG laser without any mask. This pattern is as the same as that of YAG 2 but Sample position is 25 mm below the laser focus. As it is clear in the figure the spots have a lot of dark areas which could be attributed to over exposure and graphitization. The spots' diameter and distance between them are approximately 90µm and 100µm, respectively, and they include about 17% of the total area.

Studies have shown that crystallinity could be observed in the W-S-C sputtered coatings with low C content and this crystalline structure would be progressively lost with increasing C content. In XRD diffractograms of pure WS or low C content WS coatings, a peak could appear at around 14^{o} which corresponds to the (002) plans of the 2H-WS_2 phase due to the reorientation of the basal planes parallel to the coating surface. In addition, the broad peak between 30-40 degrees often contains 100, 101, 102 and 103 planes of tungsten disulphide. The lateral dimension of the basal planes would be declined by increasing C content which results in broader and less intense peaks and this trend could continue until a broad peak corresponding to an amorphous structure is observed [69].

Figure 12(a) illustrates the X-ray diffractograms of the samples treated by YAG laser along with untreated sample as a reference. Since the C content is about 50%, so, it has not been expected to observe a broad peak in the diffractogram of untreated sample. However, there is no any distinct and intense peak in diffractograms of YAG-laser-treated samples. Although, Raman spectroscopy has confirmed that some areas on treated samples have been crystallized and the peaks corresponding to WS_2 appear in

their spectra; but it seems that the crystallization of WS_2 could not be observed by the XRD technique, due to small size of the crystals

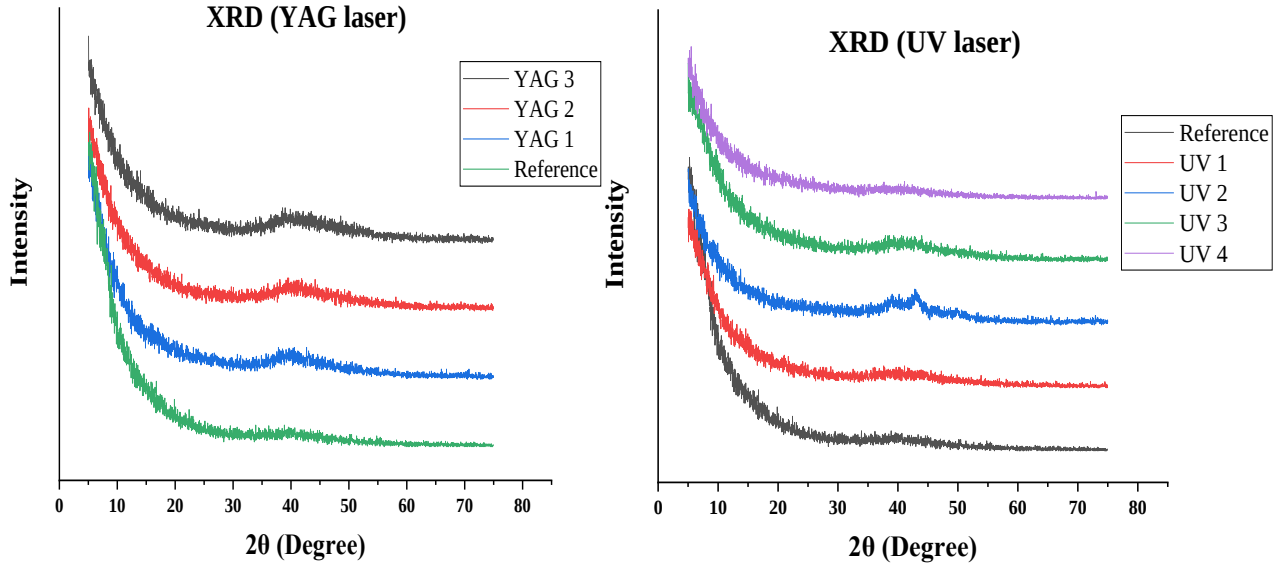

(a) (b)

Figure 12. The XRD patterns of samples treated by (a) YAG and (b) UV laser.

As mentioned before, less than 20% of samples' surfaces were treated by YAG laser and also whole the treated area does not necessarily consist of WS_2 crystalline structure; so, it is very likely the crystals are too small to be detected by the technique.

The diffractograms presented in Figure 12(b), are related to samples treated by UV laser and as it is obvious all samples, except UV 2 have more or less the same XRD patterns which consist of a broad peak without any distinct and intense peak. This confirms the existence of an amorphous structure and probable changes in the structure do not have a significant effect on diffractograms. Based on Figure 12(b), XRD pattern of UV 2 shows a relatively intense peak at $2\theta \sim 43^{o}$, it could be attributed to graphite due to over exposure. It is worth noticing that over 70% of this sample's surface was treated by UV laser and therefore the amount of this material is probably large enough to appear as a peak in the diffractogram.

Figure 13 shows the Raman spectra of three different points on surface of the UV 1 and reference (the untreated sample) along with its optical microscopic picture. When nanocrystalline graphite changes into amorphous carbon, G peak moves from 1600 cm^{-1} toward 1510 cm^{-1} and the $I(D)/I(G)$ ratio decreases; Increasing dispersion of the G peak, also, occurs [70]. Raman spectroscopy can be used, as an efficient method, for the chemical identification and the structural analysis of WS_2 and carbon. Table 5 shows band positions of 2H-WS_2 single crystals, D and G bands of carbon [71, 72].

Table 5. The band positions of the WS2 and carbon.

category	band	Wavelength (cm^{-1})
2H-WS_2	A1g	421
	E2g	356
	E1g	306
	LA(M)	176
Carbon	G	1560
	D	1385

All spectra, presented in Figure 13 show peaks at wave number 356 and 421 cm^{-1} corresponding to WS_2 and two other peaks at 1385 and 1560cm^{-1} assigned to D and G bands of carbon, respectively. Appearance of peaks 356 and 421 cm^{-1} justifies the crystallization of WS_2 in the structure which might result in better tribological performance. On the other hand, moving of G peak from 1581 to 1600 cm^{-1} and increasing of $I(D)/I(G)$ ratio would prove the graphitization of the structure [70]. According to Figure 13, both Point 22 and Point 42, which are brighter than Point 21, demonstrate WS_2 peak, and D peak shoulder at around 1385.7 cm^{-1}. By comparison between Point 21 and the reference, it is evident that $I(D)/I(G)$ ratio increase and G peak shifts to 1600cm^{-1}, which means an increase of sp2 content in the film associated with the progress of graphitization. So, by approaching to pulse centre, the crystallization of the TMD phase is not pronounced, while increased graphitization occurs.

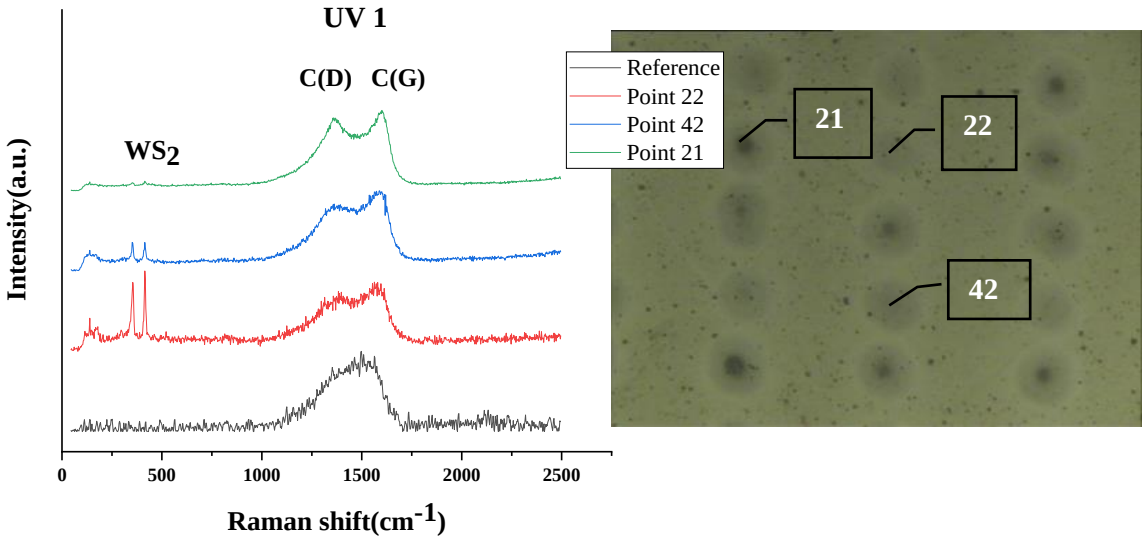

Figure 13. The Raman spectra of UV 1 along with its optical microscopic pictures.

Figure 14 illustrates the Raman spectra from dark and bright areas on UV 2, hatched using UV laser. As it is obvious in the figure, the peaks related to WS_2 appears in the Raman spectra.

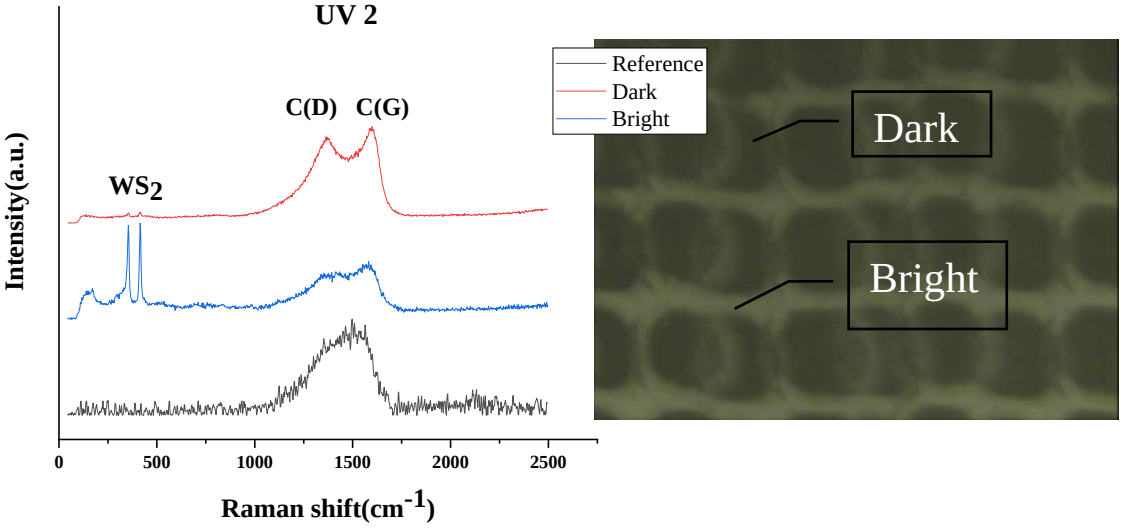

Figure 14. The Raman spectra of UV2 along with the optical microscopic picture of UV 2.

However, the WS_2 peaks in the bright areas are more intensive than those in the centre of dots. WS_2 crystallized area in this sample could contribute in providing low friction; although, as mentioned earlier, more than 70% of the surface consists of dark spots which are suspicious of graphitization due to over exposure. So, it is expected that this sample would no fulfil the requirements.

The sample UV 3 consists of the parallel lines which has some dark and bright parts (Figure 14). The dark spots in exposed areas have no special peaks related to WS_2, while the light areas show very weak peaks at wave number 356 and 421 cm^{-1} corresponding to WS_2 and two other peaks at 1360 and 1585cm^{-1} assigned to D and G bands of carbon, respectively. The spectra not only do not demonstrate any significant peaks corresponding to WS_2, but also the $I(D)/I(G)$ ratio increases and G peak shifts towards 1600cm^{-1}, which as mentioned before it signifies that the amorphous carbon within the structure was graphitized.

Figure 15 illustrates the Raman spectra from dark and light areas as well as intersecting point on UV 4. The Raman spectra in dark and bright areas are more or less similar to those of in UV 3. Furthermore, in intersecting area, there is no peak related to WS_2 which could be as a result of over exposure. On the other word, the D and G peaks are well-separated, indicating $I(D)/I(G)$ ratio has increased, probably owing to graphitization.

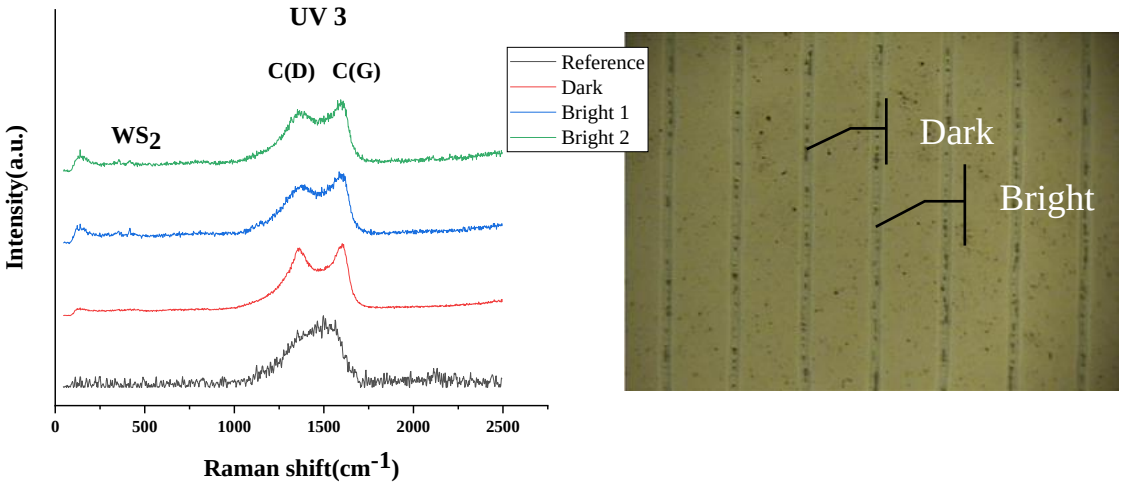

Figure 14. The Raman spectra of UV 3 along with the optical microscopic picture.

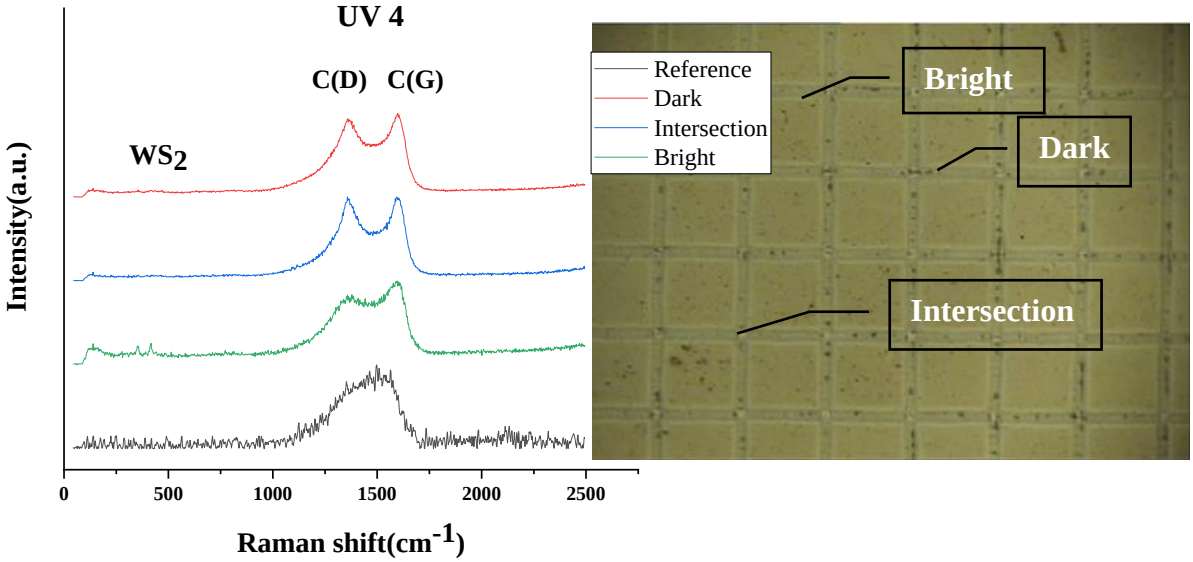

Figure 15. The Raman spectra of UV 4 along with the optical microscopic picture.

Figure 16 shows the Raman spectra of four randomly selected areas on the surface of YAG 1 along with the spectrum of reference sample. As it is obvious in the figure, two distinct peaks at wave number 356 and 421 cm^{-1} appear which correspond to WS_2. In addition, the D peak has relatively shouldered around its position and moving G peak toward 1600cm^{-1} which means slightly graphitization in structure. All in all, the WS_2 peaks are more intensive than D and G peaks and it is predicted the sample would be among the candidates with the improved tribological performance.

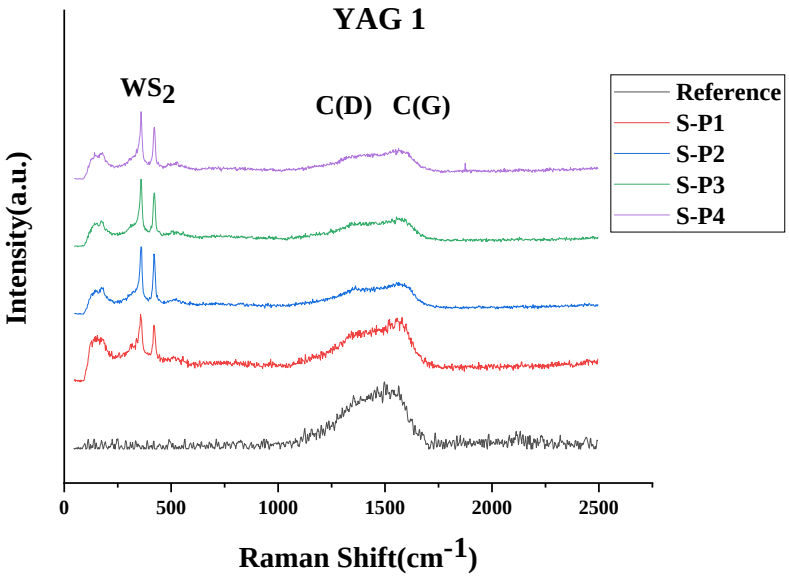

Figure 16. Raman spectra of four spectra randomly collected from YAG 1 along with reference sample.

Figure 17 corresponds to Raman spectra of YAG 2 as well as its optical microscopy picture. The red crosses correspond to the spots where Raman spectra was collected. In addition, S5 is only used for comparison which has approximately the same spectrum as the reference sample.

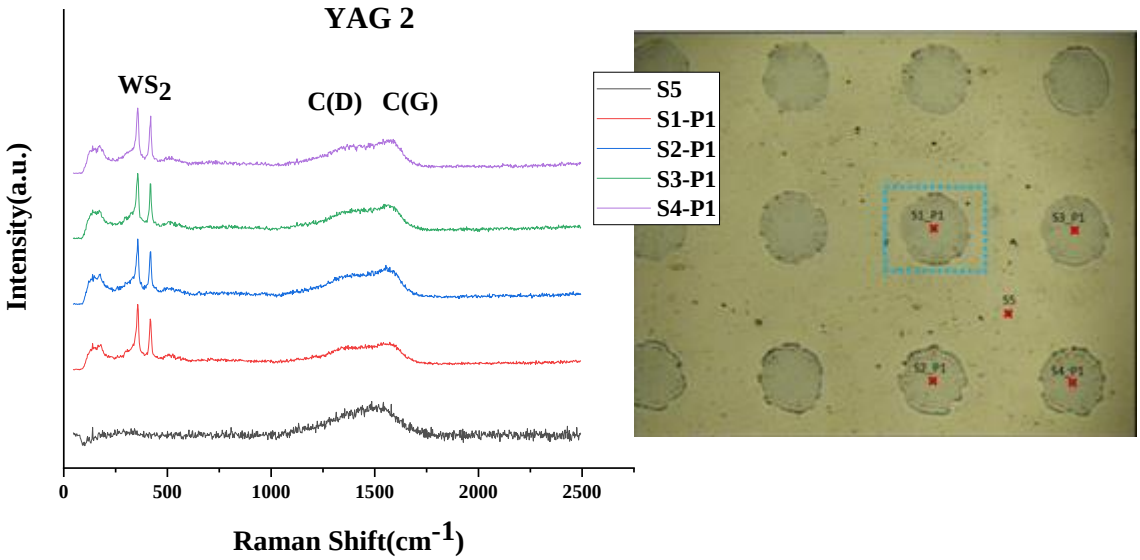

Figure 17. Raman spectra of four spectra randomly collected from YAG 2 as well as optical microscopy picture taken with a 10x lens.

According to table 2, one of the main differences between YAG 1 and YAG 2 is the use of the mask in the YAG 2. As expected, the phase transformation was also promoted and the average intensity ratio of the two dominant peaks (I_{356}/I_{421}) seems similar for both samples. Thus, the characteristics of spectra in YAG 2, namely the peak position and peak intensity is mostly as the same as those of in case of YAG 1.

The sample position height was then reduced by 5 mm, meaning that YAG 3 was irradiated closer to the focus position compared to YAG 2. As before, the red crosses correspond to the spots where Raman spectra was collected. Given that the different diffraction patterns are more visible in this sample, darker and brighter areas were separately measured with Raman spectroscopy in order to understand the difference in their chemical composition. Figure 18 corresponds to the Raman spectra taken at the centre of four consecutive spots, as represented in its optical microscopic picture. As seen in the Figure 18(right), there is higher heterogeneity among the spots, which might be due to the sample composition and thickness variations. In terms of graphitization, it seems to be similar among the spots investigated, with the difference being the presence of more crystalline WS_2 phase in some of the spots, and the absence of WS_2 peaks in others.

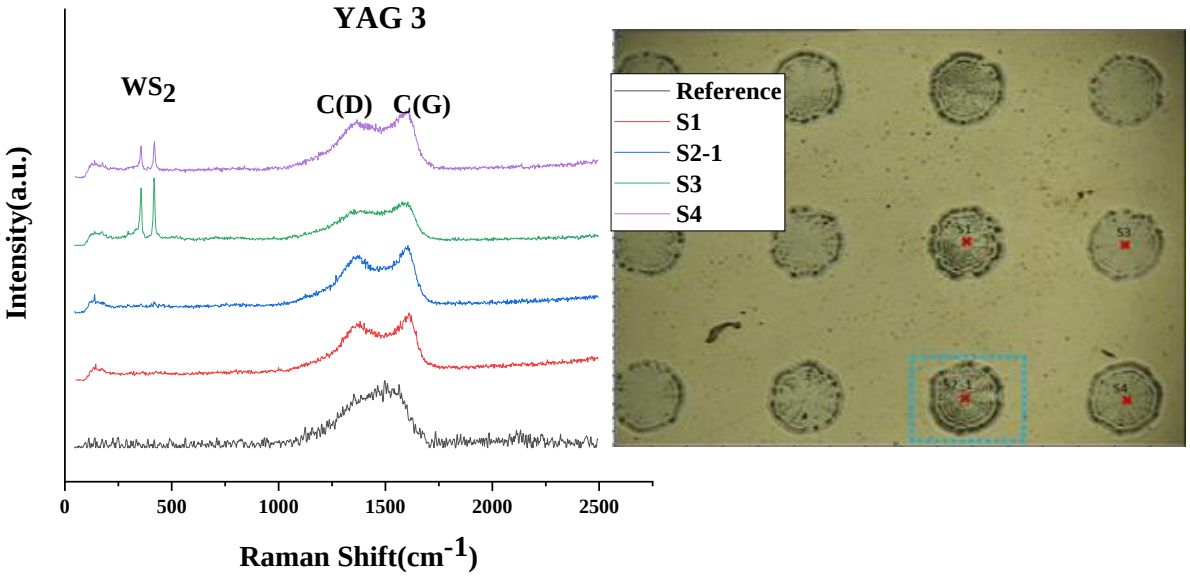

Figure 18. Raman spectra of the S1, S2-1, S3 and S4 spots on YAG 3.

The results plotted in Figure 18 demonstrate that the peaks at 356 and 421 cm^{-1} are barely present in S2-1 and S2-3, and completely vanished in S2-2 (darker area). In the darker areas, a higher graphitization is observed.

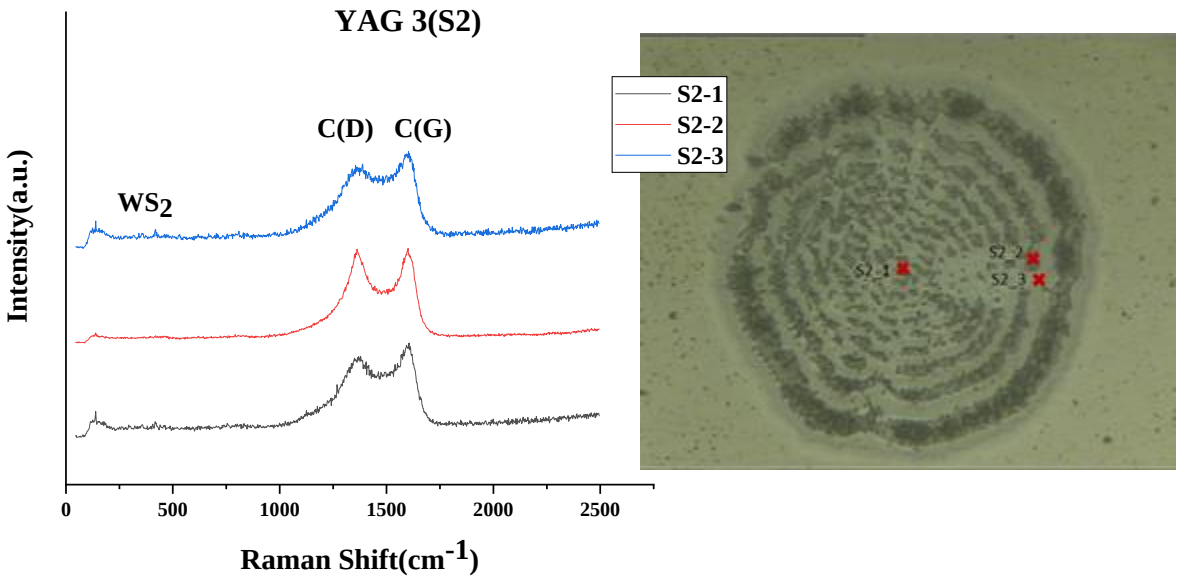

Figure 19. Raman spectra taken at the areas of the red crosses in Figure 18.

Mechanical properties of studied samples were evaluated by depth-sensing nanoindentation technique, listed in Table 6. In addition, Figures 20 and 21 illustrate the comparison of hardness (H) and reduced Young's modulus (E) values for each sample, treated by UV laser in different areas including irradiated spots and free surfaces. It is clear that irradiated areas have the lower values of hardness than those in the free surfaces; which means that the treatment has decreased the hardness. In addition, UV 2, has the smallest amount of hardness in both irradiated and free areas.

Table 6. The mechanical properties of the samples treated by UV laser.

Sample	Area	Hardness (MPa)	Standard deviation	Modulus (MPa)	Standard deviation
UV 1	Free surface	5.3	0.3	85	2
	Points	4.3	0.2	69	2
UV 2	Free surface	3.4	0.5	72	5
	Points	3.0	0.4	69	4
UV 3	Free surface	5.1	0.2	83	3
	Line	4.1	0.7	69	4
UV 4	Free Surface	5.0	0.3	84	4
	Line	4.8	0.1	76	2
	Cross Line	3.3	0.2	69	3

As mentioned before, more than 70% of its surface has been treated by the laser and the irradiated area has been, to some extent, either graphitized or oxidized due to over exposure. The low value of hardness in free surface, also could be related to closeness of this area to irradiated spots. Furthermore, since this sample has a very compact pattern, so the loading/unloading cycles in about 20 different zones have dispersed.

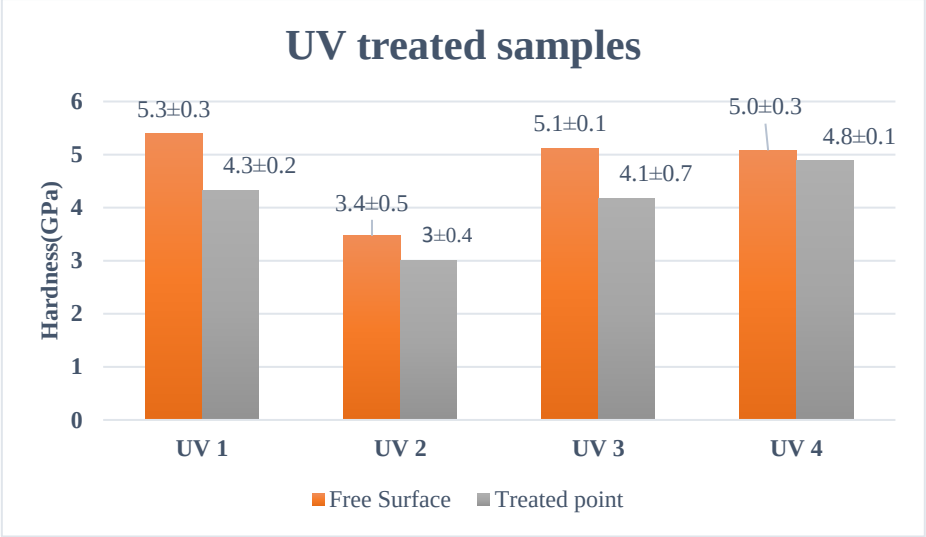

Figure 20. The comparison of hardness values between free surface and irradiated area of samples treated by UV laser.

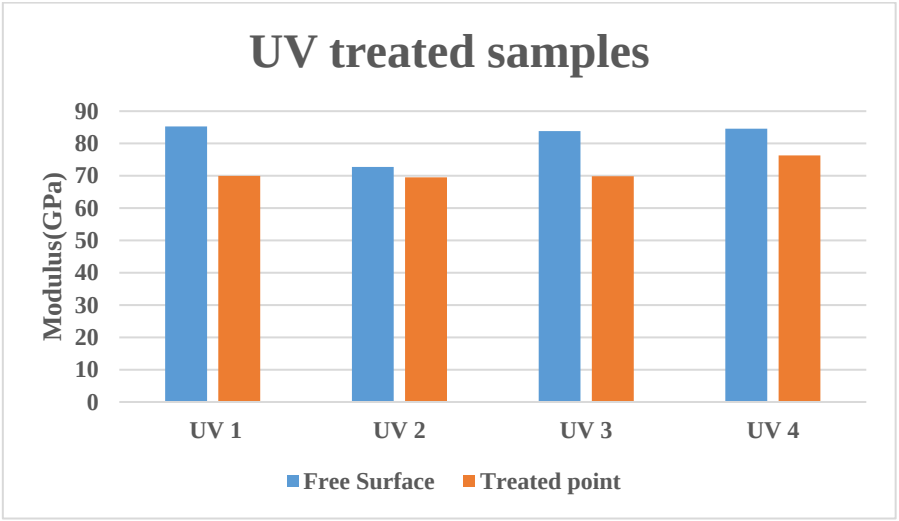

Figure 21. The comparison of Modulus values between free surface and irradiated area of samples treated by UV laser.

By considering the Standard deviations, UV 1, UV 3 and UV 4 have very similar hardness values in irradiated and free areas. However, intersecting areas of UV 4 have undergone a declining in hardness value to 3.35 MPa, probably owing to over exposure. Except UV 2, there is no big difference in hardness values between free and irradiated areas of other samples and they can be still assumed as a desirable coating. Moreover, according to Figure 21, the values of modulus have approximately the same trend as hardness of UV treated samples.

Table 7 presents the mechanical properties of the YAG-laser treated samples, evaluated by depth-sensing nanoindentation technique. In addition, Figures 22 and 23 illustrate

the comparison of hardness (H) and reduced Young's modulus (E) values for each sample in different areas including irradiated spots and free areas.
It is worth to mention that since the YAG 1 has no pattern for treatment and was treated by random dots, so there is no data for the free surface and the untreated sample has been taken as the reference to compare.

Table 7. The mechanical properties of the samples treated by YAG laser.

Sample	Area	Hardness (MPa)	Standard deviation	Modulus (MPa)	Standard deviation
YAG 1	treated	4.9	0.4	71	2
YAG 2	Free surface	5.3	0.2	85	2
	Points	5.0	0.5	75	4
YAG 3	Free surface	5.1	0.2	83	2
	Line	2.4	0.4	58	5
Reference	Untreated	5.2	0.3	84	4

As it is obvious in Figure 21, the hardness values of irradiated areas in YAG 1 and YAG 2 have not been dropped significantly and generally these coatings are still as hard as before treatment. In case of YAG 3, the hardness value has been approximately halved in treated areas which could be attribute to reduce the distance between sample and laser gun, meaning that YAG 3 is irradiated closer to the focus position compared to YAG 2. So, the irradiated area has been graphitized which could lead to decline in hardness.

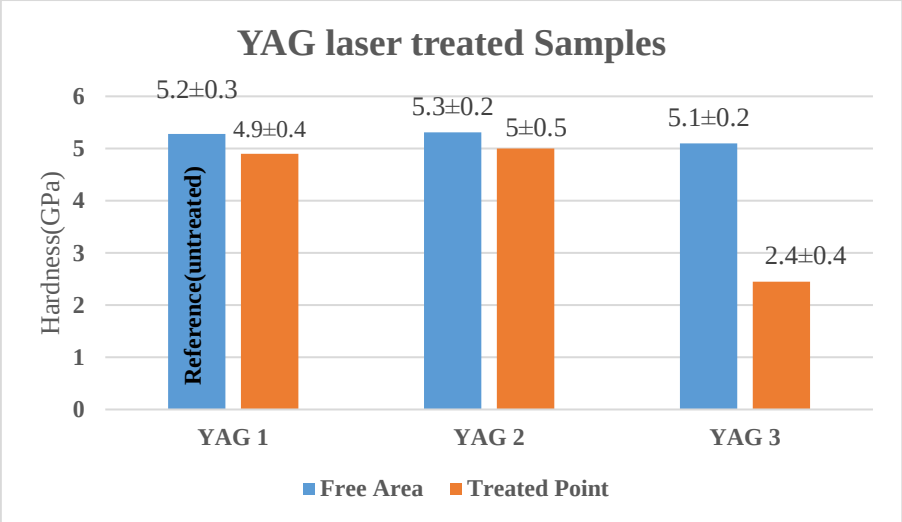

Figure 22. The comparison of hardness values between free surface and irradiated area of samples treated by YAG laser.

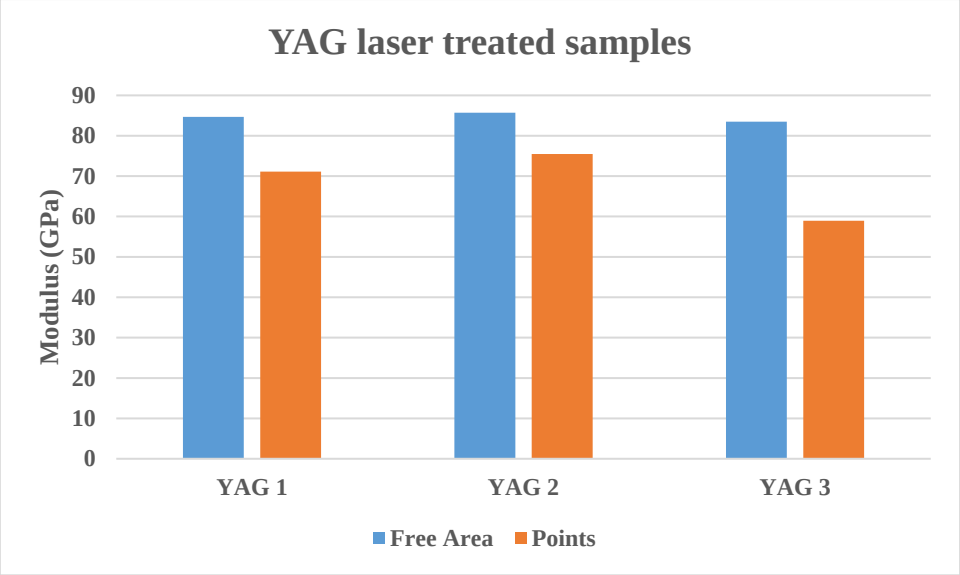

Figure 23. The comparison of Modulus values between free surface and irradiated area of samples treated by the YAG laser.

From tribological point of view, the formation of a tribolayer is introduced as the mechanism of self-lubricating in a WS_2 coating. There are several factors which can affect tribological efficiency of the coating including the nature of the material and the surface, environment, the contact geometry, load and so on. As the one of main objectives of this work is the investigating of tribological performance of the laser treated W-S-C coating, so the reciprocating ball-on-disk machine was employed to measure friction coefficient of the coating during sliding.

Figure 24 shows the evaluation of the friction coefficient versus time in the samples, treated by UV laser as well as reference sample. Generally, there are two main stages for sliding process of the thin films, namely running-in and steady-state sliding. In the running-in stage, the friction coefficient of reference sample is the highest with COF value of 0.15, continuously dropping towards a steady-state value of ~0.08. In case of UV 1, after running in stage, it decreased and increased in first 100 seconds and it levelled out approximately until the end of the test. Its fiction coefficient was lower than that of reference and then they tend to converge towards a similar value by the end of the test. As shown in Figure 25, the spots on UV 1 were gradually faded due to sliding and consequently the ball reached the untreated depths of the coating; so, it would be reasonable to have the same friction coefficient. The friction coefficient of UV 2 rose abruptly during running-in phase and it remains approximately in the same rang around 0.1. It is worth to mention that after first few second, the friction coefficient of UV 2 became more or less as the same values as friction coefficient of reference until around 355 second and then the friction coefficient of UV 2 had slightly higher value compared to the reference. In addition, Figure 25 confirms that a considerable amount of treated layer in UV 2 had been removed by sliding, which probably results in higher wear rate.

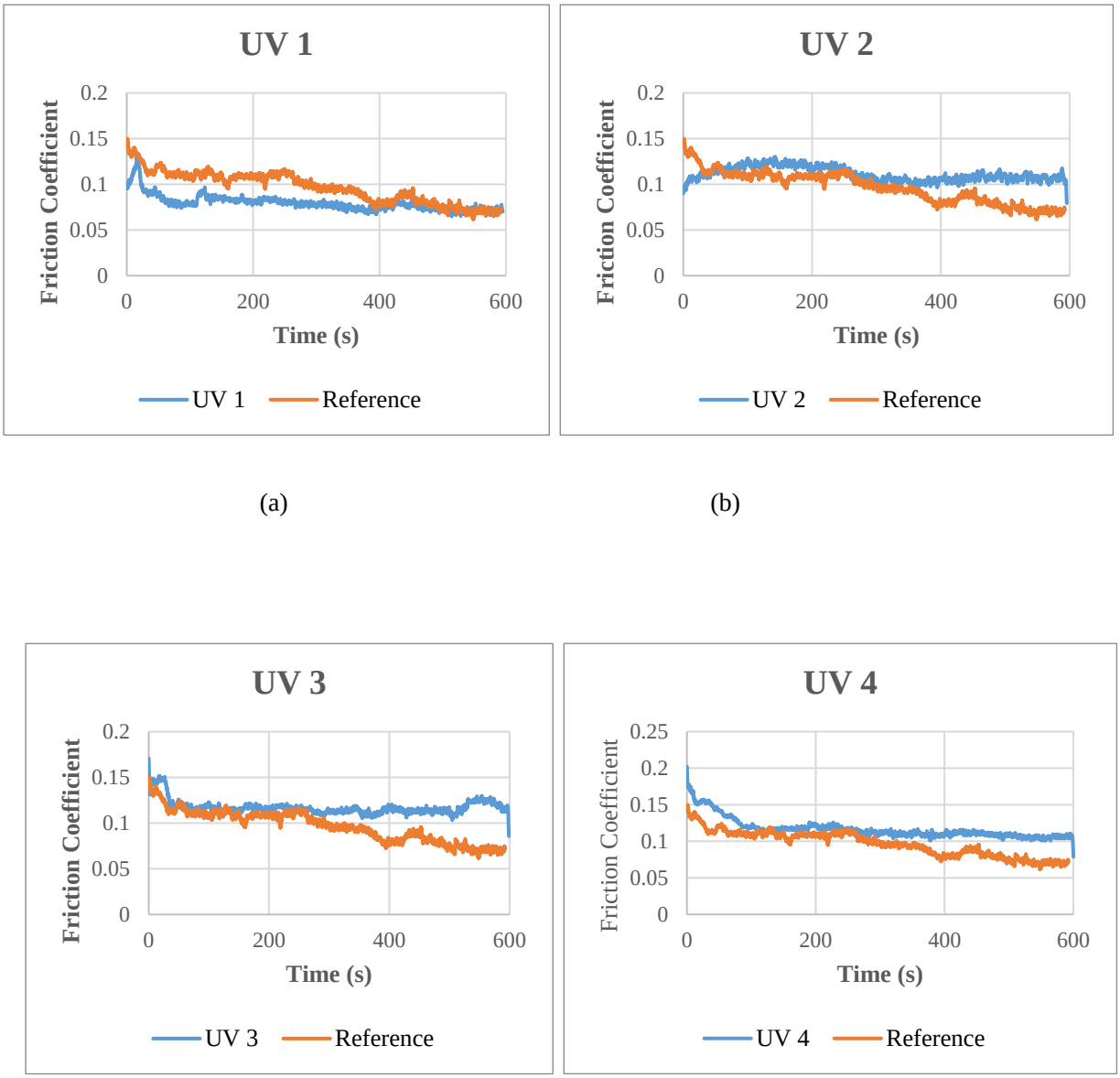

Figure 24. The friction coefficient versus sliding time in the UV-laser treated samples.

Despite some small differences, both UV 3 and UV 4 show the same trends; however, after about 250 second the friction coefficient values of UV 3 are slightly higher than those of for UV 4. Figure 25, also confirms that the treatment spots cannot be observed in the middle parts of the wear scar, owing to the sliding.

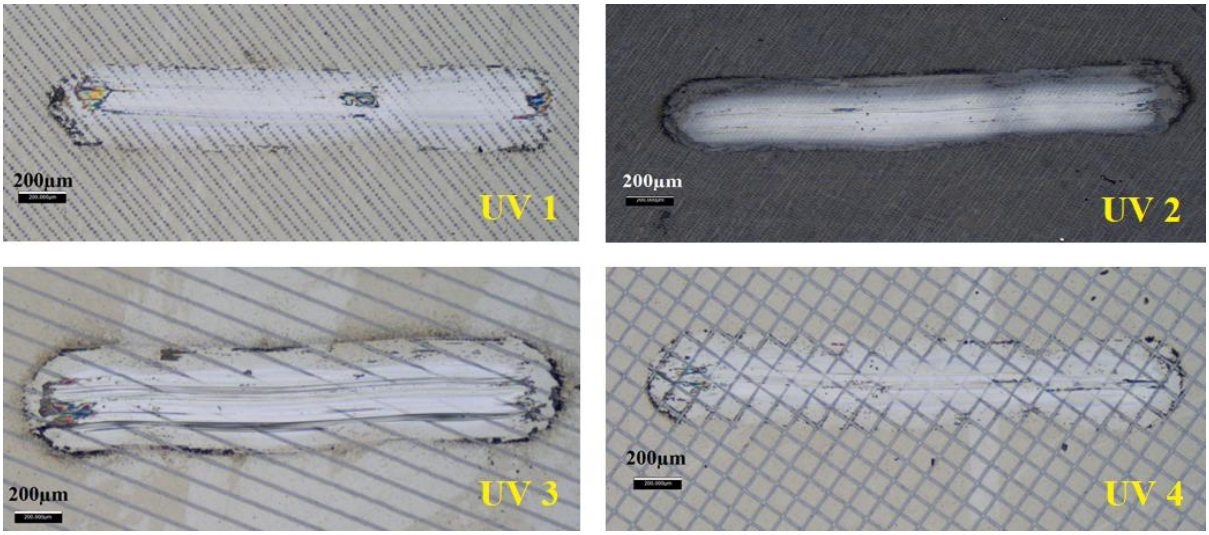

Figure 25. The optical microscopic pictures of the scars on UV-laser treated samples.

Figure 26 illustrates the friction coefficient curves of the samples, treated by the YAG laser, during sliding. It is noticeable that YAG 1 and YAG 2 tend to undergo the same trends, so that before 400 second their friction coefficients are lower than reference and after that they all have approximately the same friction coefficient values. Friction coefficient of YAG 3 fluctuated during the running in stage and then stabilized until the end of the test; although, in some periods, the YAG 3 graph overlapped the reference graph.

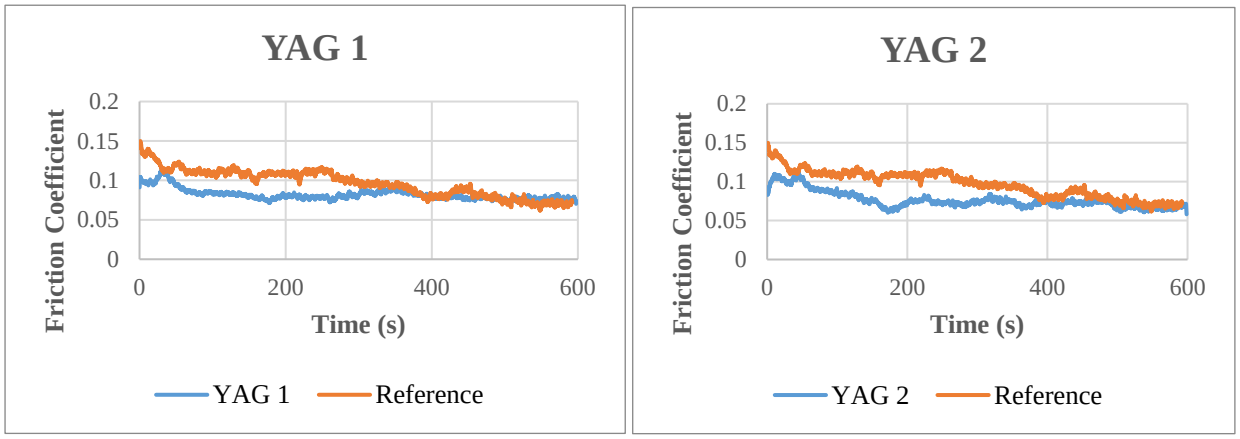

(a) (b)

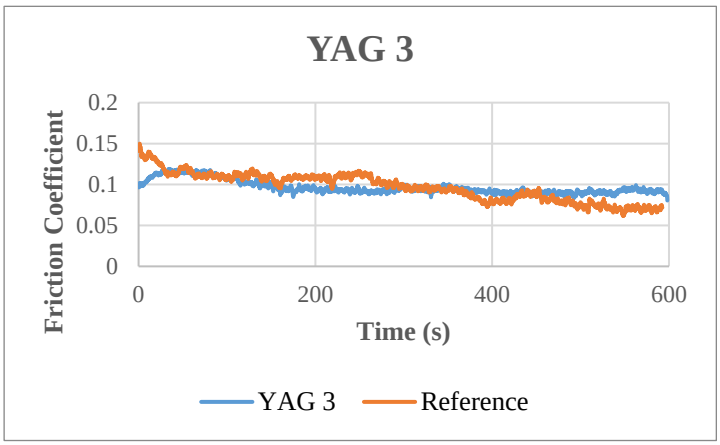

(c)

Figure 26. The friction coefficient versus sliding time in YAG-laser treated samples.

According to Figure 27, in case of YAG 1, it seems that the treated layer has been removed by the ball; it could be why it reached at as the same friction coefficient as the reference after about 6 minutes. Figure 27, also, illustrates that some treatment spots in the scar on YAG 2 totally disappeared, while despite some changes, the spots are still visible on YAG 3. This could be attributed to increase in laser penetration due to reducing the distance between the laser gun and the sample in YAG 3.

According to Figure 27, in case of YAG 1, it seems that the treated layer has been removed by the ball; it could be why it reached at as the same friction coefficient as the reference after about 6 minutes.

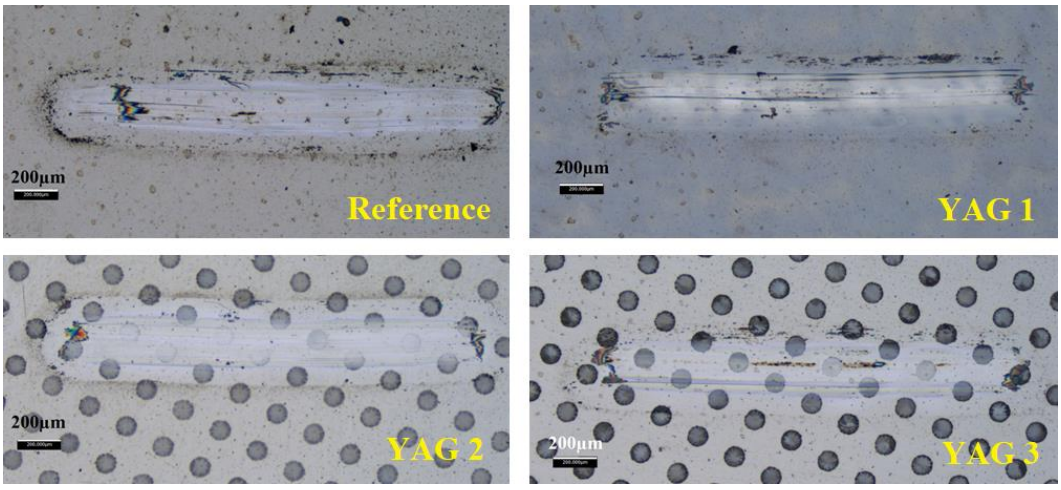

Figure 27. The optical microscopic pictures of the scars on UV-laser treated samples.

The Table 8 illustrates the average friction coefficients of UV-laser treated samples along with their wear rates, calculated by the Archard equation. As it is mentioned earlier, the wear rates were calculated after getting the scar profiles in three different

areas namely its left, middle and right parts using the profilometer and then averaging them. According to Table 8, UV 1 has by the far the lowest friction coefficient and wear rate among the UV-treated samples and its friction coefficient is also lower than the reference; however, the wear rate of this sample is slightly higher than the reference. It seems that the laser power, used to treat this sample, has been, to some extent, in the acceptable range, resulting in WS_2 crystallization and COF reduction.

Table 8. The average friction coefficient and wear rates of samples treated by UV laser.

Sample	Average CoF	Wear rate (mm^3/mN) $\times 10^{-7}$
UV 1	0.08±0.01	3.8±0.1
UV 2	0.11±0.02	8.5±0.3
UV 3	0.12±0.02	5.6±0.9
UV 4	0.12±0.04	4.2±0.4
Reference	0.1±0.01	3.6±0.9

On the other hand, UV 2 has the highest wear rate among the all samples, which can be due to accelerated removal of the upper graphitized layer during sliding. It is worth to mention that this sample had the lowest hardness, according to Table 6. None of UV 3 and UV 4 shows desirable tribological properties. This could be attributed to their either high laser power or pattern. Although, the wear rate of UV 4 is lower than that of UV 3, maybe as a result of bigger laser-treated area in case of UV 4.

Table 9. The average friction coefficient and wear rates of YAG-laser treated samples.

Sample	Average CoF	Wear rate (mm^3/mN)$\times 10^{-7}$
YAG 1	0.08±0.02	3.8±0.1
YAG 2	0.07±0.01	2.9±0.8
YAG 3	0.09±0.01	4.9±0.1
Reference	0.1±0.01	3.60±0.9

Furthermore, the calculation of average friction coefficients and wear rates in case of the YAG-treated samples presents very interesting results. According to Table 9, not only among the YAG-laser treated samples, but rather among all samples, YAG 2 has the lowest friction coefficient and wear rate. In addition, the average friction coefficient of YAG 1 is also, lower than that of the reference. However, its wear rate is slightly higher than the reference.

These two samples, namely YAG 1 and YAG 2 had WS_2 crystallization in their structures due to the laser treatment which reduced their friction coefficients during running-in and some part of steady-state stages. YAG 3 has the same friction coefficient as the reference and its wear rate is higher than the reference and other YAG-laser treated samples. This high wear rate could be related to the significant reduction of its hardness owing to the treatment. Generally, the YAG-treated samples present better tribological properties than UV-treated samples.

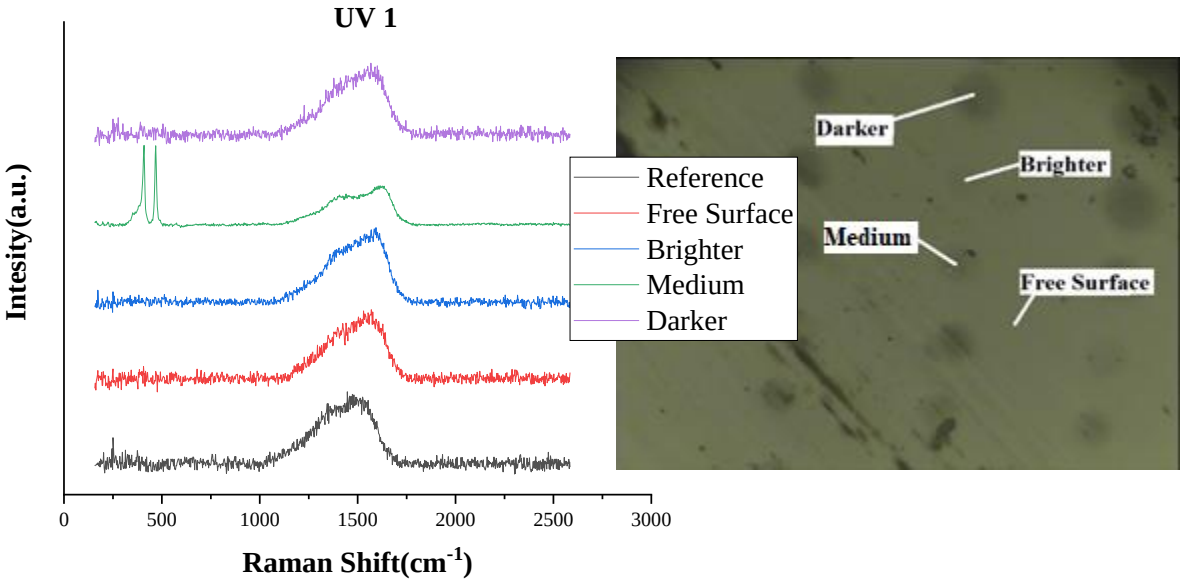

Figure 28. The Raman spectra of the scar on UV 1 after sliding along with the reference.

The Raman spectroscopy was again employed to interpret what happened in the scar area and get a better idea about tribological properties of samples. The results have been obtained from different points on the wear track and balls counterparts, as illustrated in Figure 28.

Raman spectra from different points on UV 1 as well as the reference are illustrated in Figure 28. According to the result, the untreated sample's spectrum as a reference shows an amorphous carbon structure by a broad G band around 1585cm^{-1}, which already appeared in its Raman spectrum before the tribological test.

According to Figure 28, the curve related to the medium-brightness spot has intensive WS_2 peaks and also, G and D bands related to graphitic carbon. It could justify that there are still some points which can provide lubricating properties due to their structure.

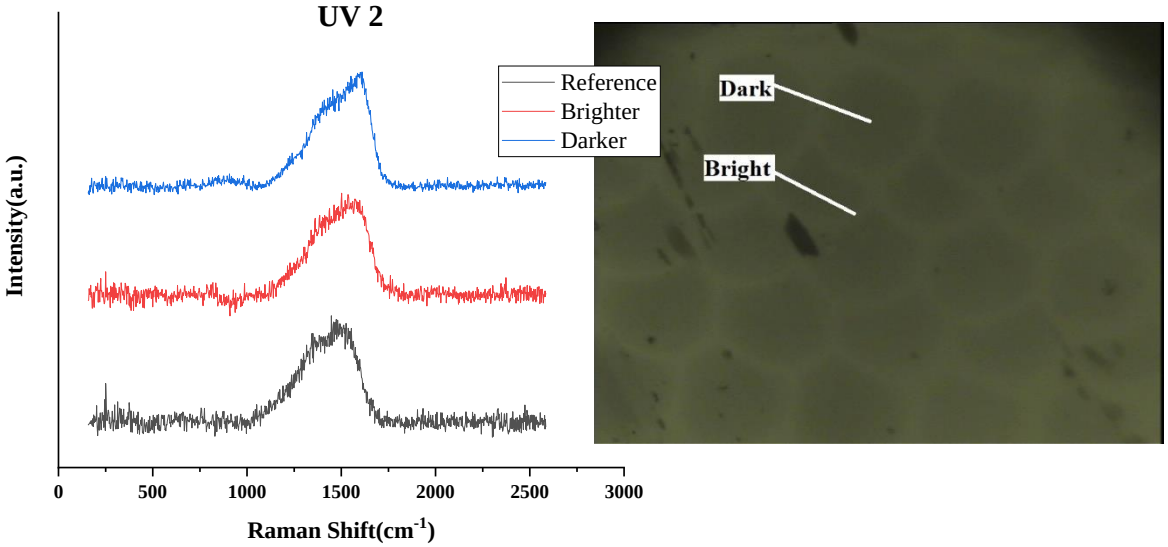

Figure 29. The Raman spectra of the scar on UV 2 after sliding**.**

As shown in Figure 29, none of area on UV 2 presents any peaks attributed to either WS_2 or graphitized carbon, regardless of existence of laser track after sliding. Based on its XRD, friction coefficient curve, nanoindentation and wear rate, it could be concluded that the upper oxide layer, which had a low hardness value, has been removed during sliding resulting high wear rate; but after removing this layer, the ball reached to a surface with, to some extent, the same characteristics as the reference.

Based on Figure 30, the Raman spectrum from bright area in laser affected line on UV 3 is similar to the reference, as being expected that the entire treated thickness was already worn out; while in dark area presents the weak WS_2 peaks and more intensive shouldered G band which had not appeared in its Raman spectra before the sliding test. In this part, the treated material was not still completely removed.

The Raman spectra from different points on UV 4 show quite strong WS_2 peaks (Figure 31). Furthermore, shouldering of D band around its position and moving G peak toward $1600cm^{-1}$ as a sign of graphitization, could confirm that in lower surfaces, it is expected to have a better self-lubricating property than upper layer; as seen previously in Figure 24(d), the friction coefficient of UV 4 dropped very slightly during sliding. It is worth noticing that these changes in spectra were not observed in its Raman spectra before sliding.

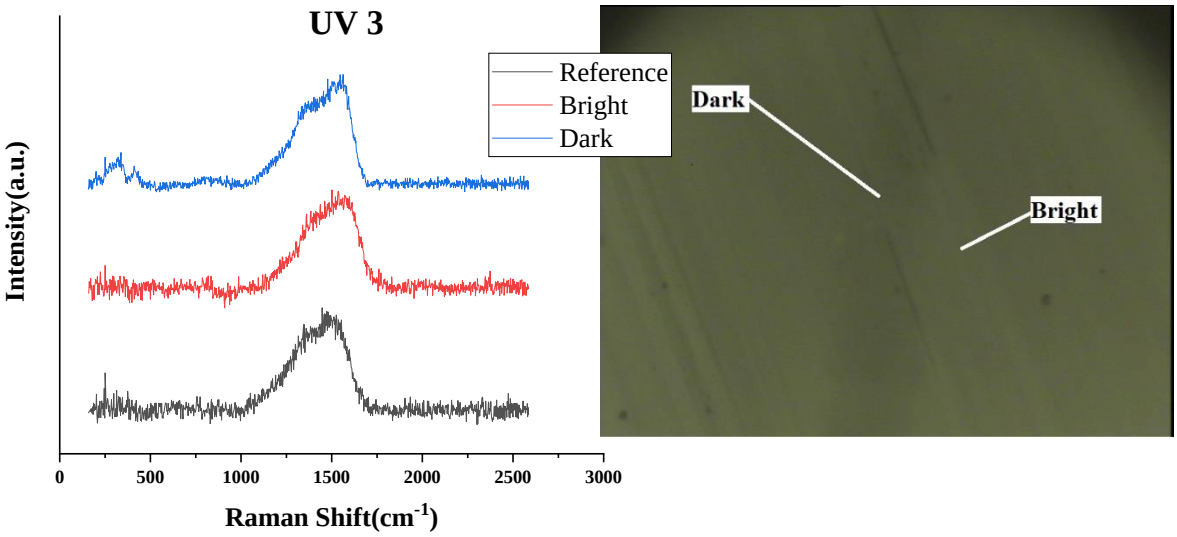

Figure 30. The Raman spectra of the scar on UV 3 after sliding**.**

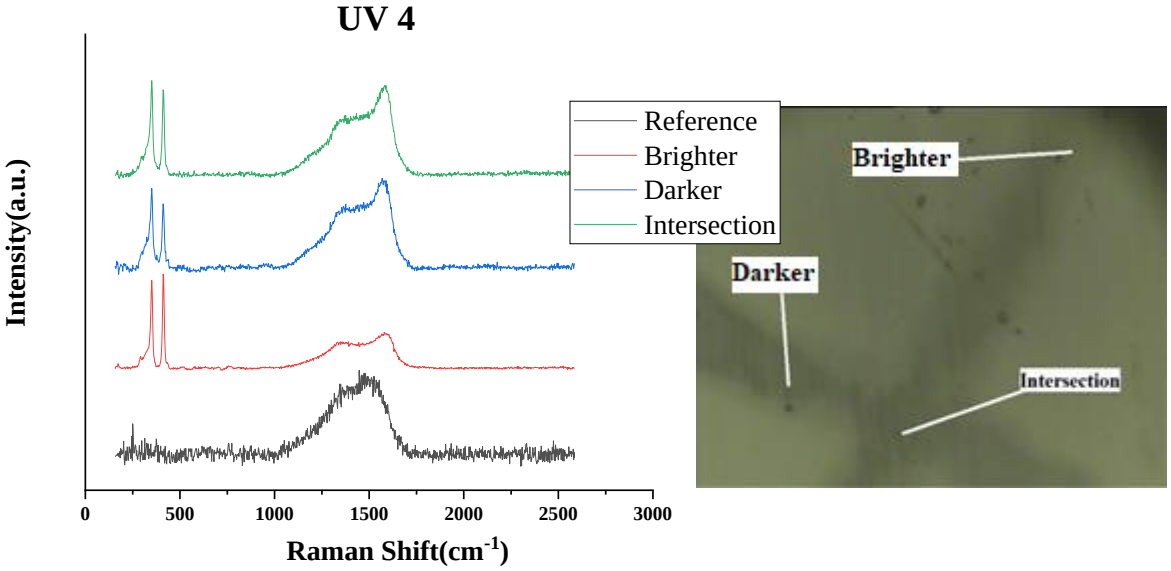

Figure 31. The Raman spectra of the scar on UV 4 after sliding.

Furthermore, as mentioned before, UV 4 has the lower wear rate than UV 3. This could be attributed to the existence of the WS_2 crystals in deeper area in UV 4, which is clear from Figure 31.

Contrary to Raman spectra of YAG 1 before the SRV test which included intensive WS_2 peaks, these peaks approximately vanished after the test and carbon peak became more and more dispersed in Figure 32, obtained from four randomly selected points on the scar. Reaching to untreated bulk materials and elimination of crystalized upper layer

would be the most possible reason which is in agreement with its friction coefficient curve, presented in Figure 26(a).

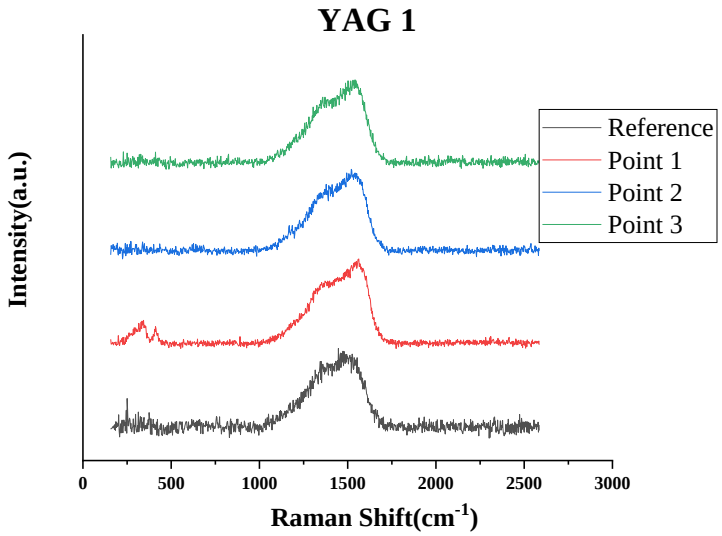

Figure 32. The Raman spectra of the scar on YAG 1 after sliding.

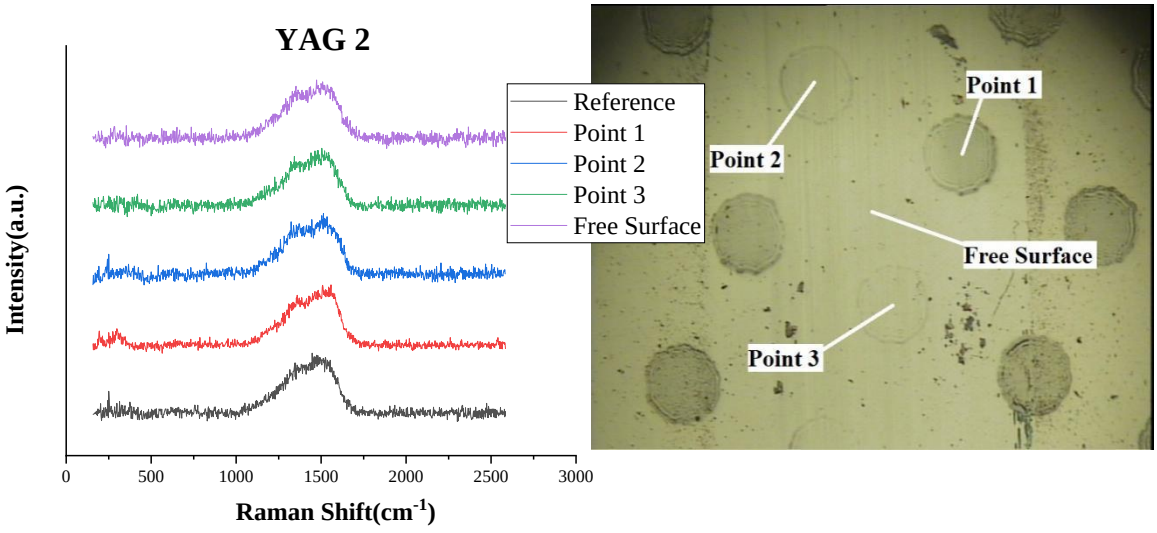

Figure 33. The Raman spectra of the scar on YAG 2 after sliding.

In case of YAG 2, As it is clear from Figure 33, there is no noticeable difference among Raman curves obtained from different areas on YAG 2 and the WS_2 peaks existed before the SRV test are completely disappeared. In fact, the treated spots did not have enough height to survive the 10-minute sliding and they have probably started to vanish after 400 seconds, based on friction coefficient curve in Figure 26(b).

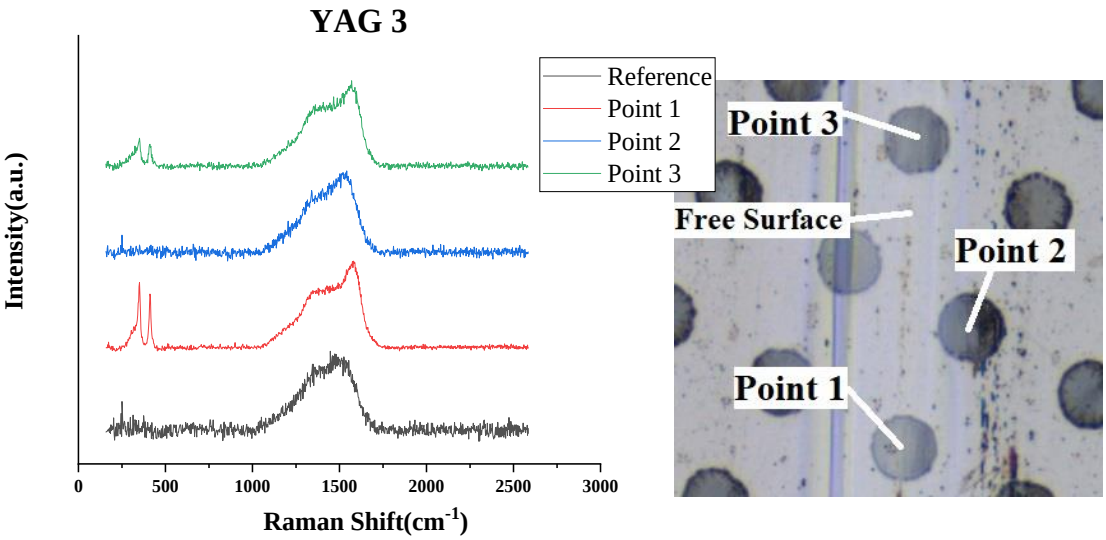

Figure 34. The Raman spectra of the scar on YAG 3 after sliding.

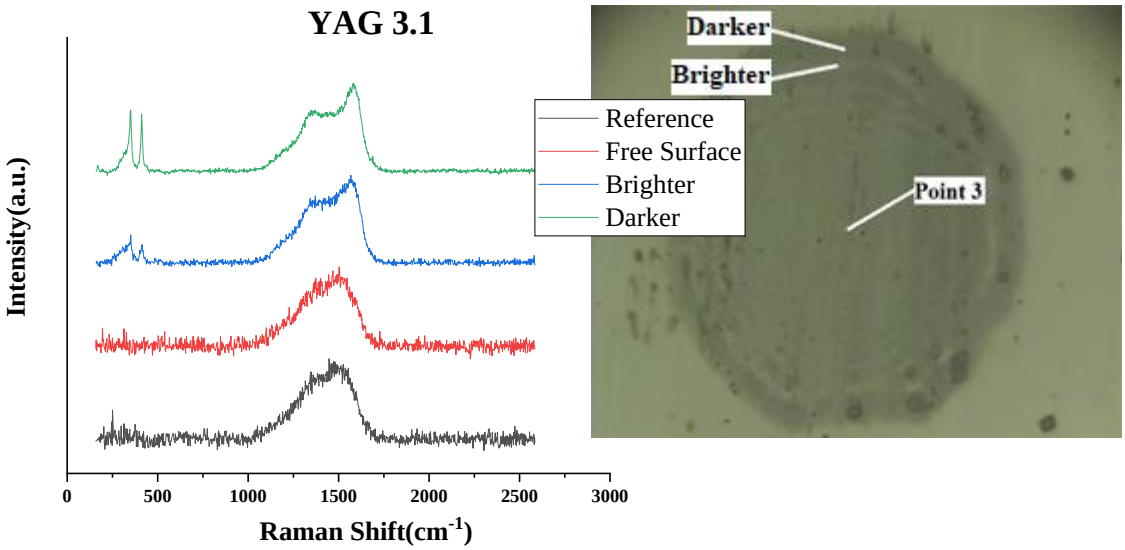

Figure 35. The Raman spectra of Point 3, presented in Figure 33.

YAG 3 was prepared by decreasing the distance between the laser gun and sample, which results in much more graphitization than YAG 2; so, it was predicted that in case of YAG 3 the laser beam penetrated deeper than YAG 2. That could be why, as illustrated in Figure 34, the scar on YAG 3 could be a combination of spots with and without WS_2 crystals. Even this combination would be found in a single treated spot; as Figure 35 presents the Raman spectra of various points from dark and bright areas of Point 3 in Figure 34. As it is obvious from Figure 35, the WS_2 peak in dark area are much more intensive than that of in bright area.

To get better understanding about treatment condition, the scheme of a typical treated sample from cross sectional view is depicted and presented in Figure 36. In this scheme, the value of 'h' is the depth of a typical spot on a sample which is filled by treated materials. Based on Figure 35, the volume of treated zone in a single spot could be divided into two parts, namely A and B. These two parts might be filled either the same materials or different ones. For example, in the case of UV 2 and YAG 3, which there were different Raman spectra before and after sliding, part A would be full of only graphitized material; which part B would be filled by mixture of graphitic carbon, crystalline WS_2 and so on.

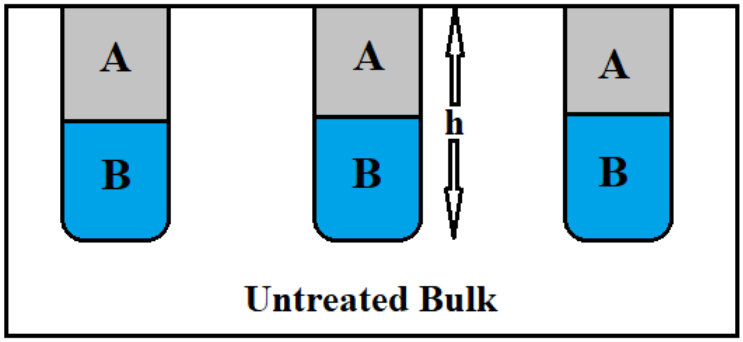

Figure 36. The schematic cross section of a typical treated sample.

As part A was removed by sliding, therefore, ball faced part B with different structure. This could happen when the sample was overexposed by the laser. On the other hand, in the cases of UV 1, YAG 1 and YAG 2, the part A and part B were probably the same and full of the crystalline WS_2. Furthermore, in these samples the laser penetrates more superficial than others; thus, after some time, the treated layer would be totally removed and the ball would reach the untreated bulk.

Table 10. The values of 'h' related to each sample.

Sample	Reference	UV 1	UV 2	UV 3	UV 4	YAG 1	YAG 2	YAG 3
h (µm)	0.36	0.38	0.91	0.70	0.37	0.36	0.35	0.49

Table 10 presents the estimated maximum depths of the scar for each sample obtained from their 2D profiles. Even, in some samples like UV 1, YAG 1 and YAG 2, it seems that comparison between Table 10 and friction coefficient curves could provide some estimations about the laser penetrating depth. These three samples also show the better tribological properties than those were graphitized in their uppermost layer.

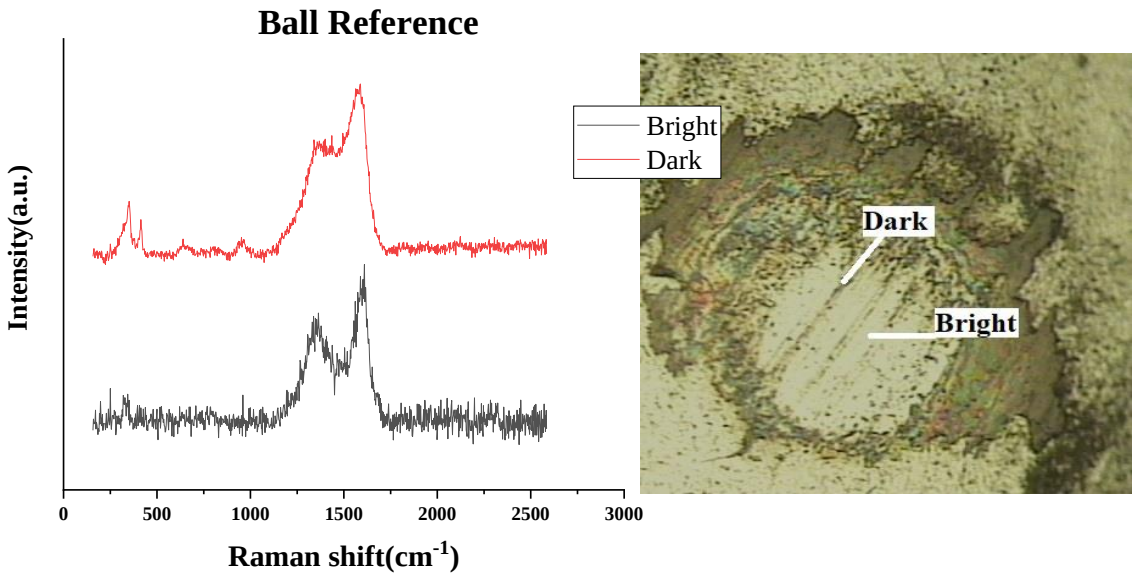

Figure 37. The Raman spectra of the ball which was in contact with the reference.

To get a better understanding about the lubricating mechanism of samples, the Raman spectra from the affected areas on each ball were obtained. Figure 37 illustrates the spectra of two different points in dark and bright areas on the reference. This sample has never received any treatment; but, due to relatively weak WS_2 peaks in dark area and increasing $I(D)/I(G)$ ratio in both areas, it could be concluded that a tribolayer has been formed on the surface of reference sample which can contribute to self-lubrication.

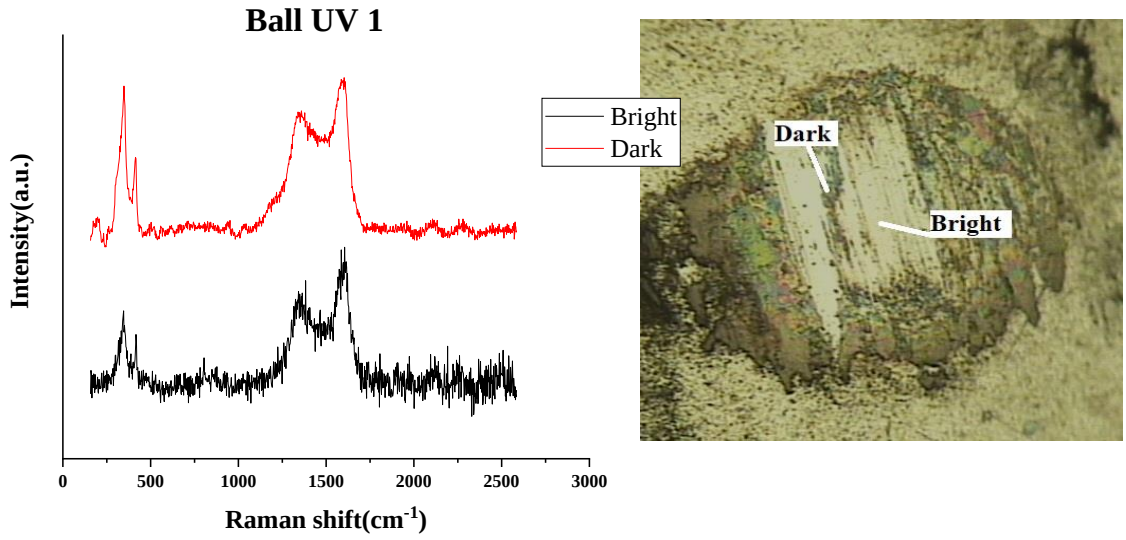

Figure 38. The Raman spectra of the ball which was in contact with UV 1.

Figure 38 confirms that the WS_2 peaks not only exist in Raman spectra of both dark and bright areas on the ball contacted to UV 1, but also, they are more intensive than those of in reference; it is also, worth noticing that since G band became narrow and D has intensified, resulting in increasing in $I(D)/I(G)$ ratio, indicating that the transfer film contains graphitic carbon.

In Raman curves of ball contacted UV 2 in Figure 39, there are WS_2 peaks and graphitic carbon peak in both dark and bright areas.

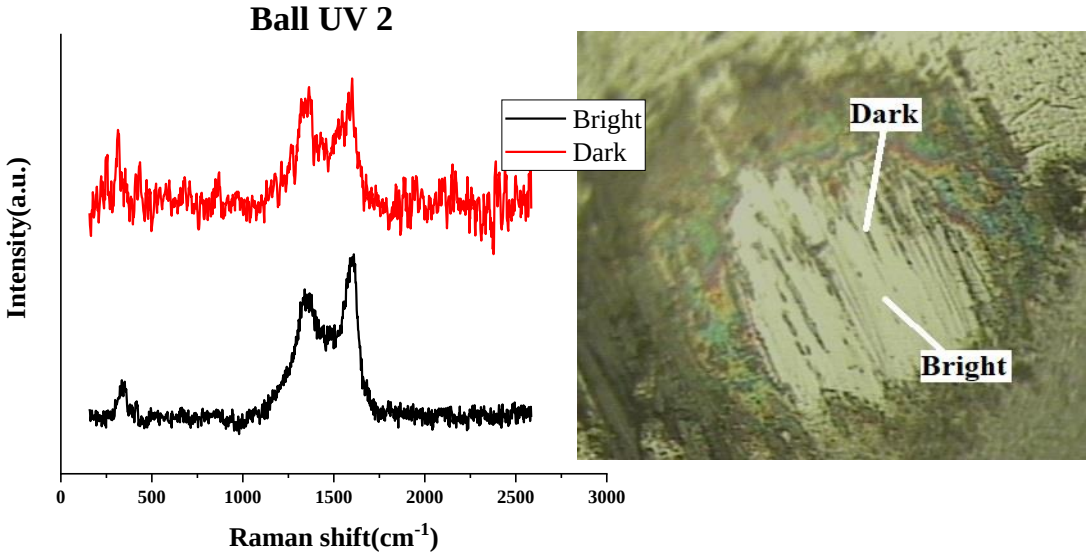

Figure 39. The Raman spectra of the ball which was in contact with UV 2.

There are some similarities between Raman spectra of the balls after testing against UV 3 and UV 4 (Figure 40 and Figure 41).

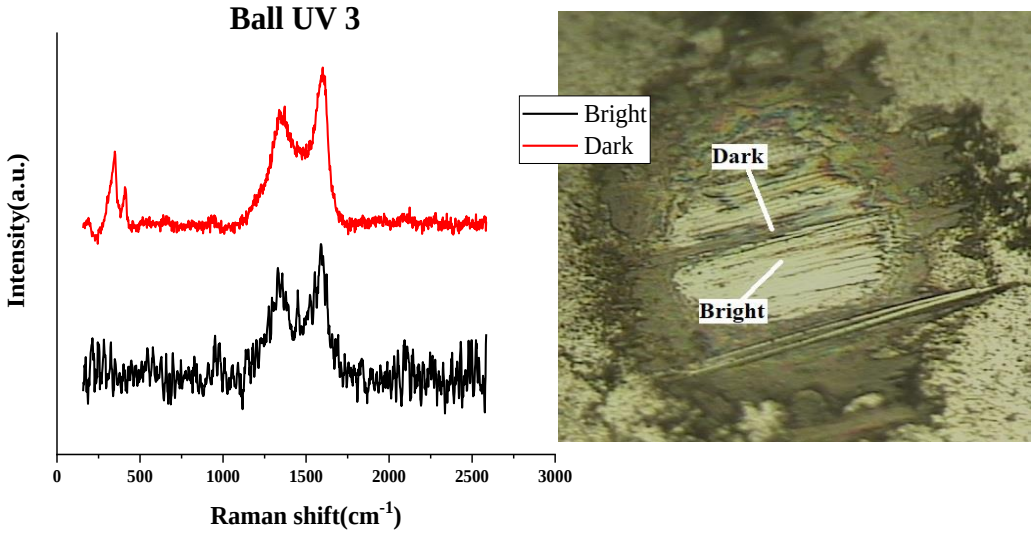

Figure 40. The Raman spectra of the ball which was in contact with UV 3.

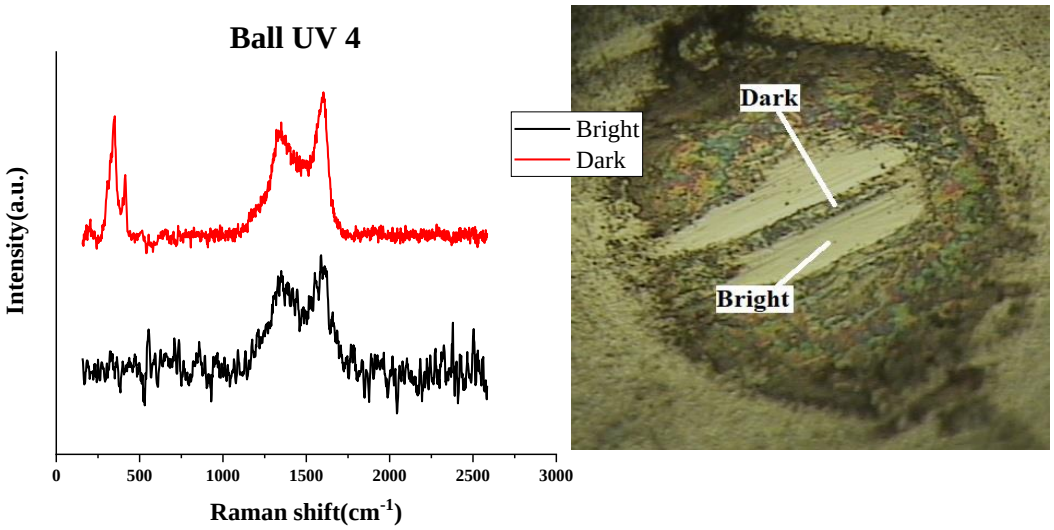

Figure 41. The Raman spectra of the ball which was in contact with UV 4.

Both balls contacted with YAG 1 and YAG 2, have, to some extent, the same Raman spectra regarding to peak position and shape. Furthermore, in each spectrum, either in dark or bright area, the G peak has shifted toward 1600cm^{-1} and D peak has appeared and therefore $I(D)/I(G)$ ratio has increased.

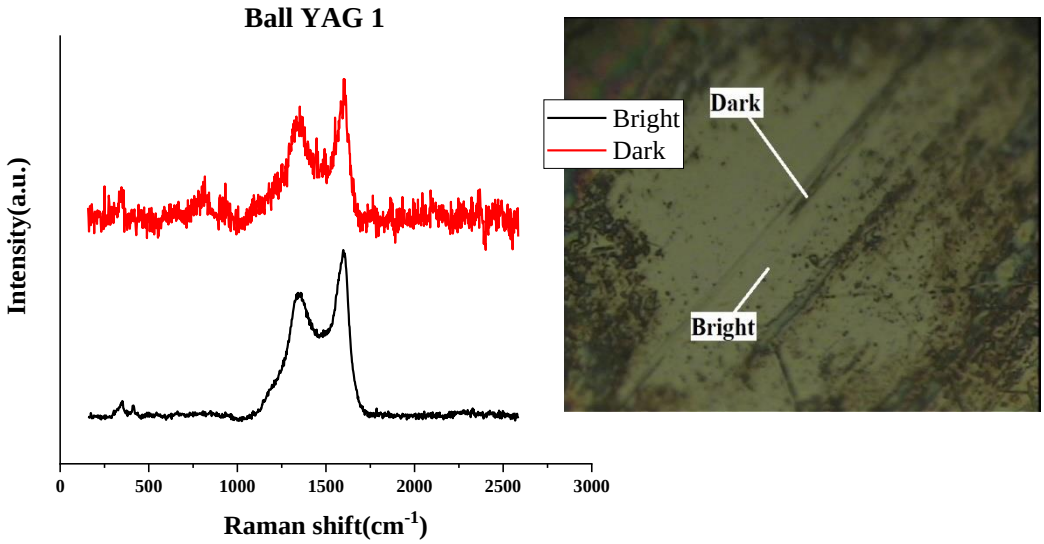

Figure 42. The Raman spectra of the ball which was in contact with YAG 1.

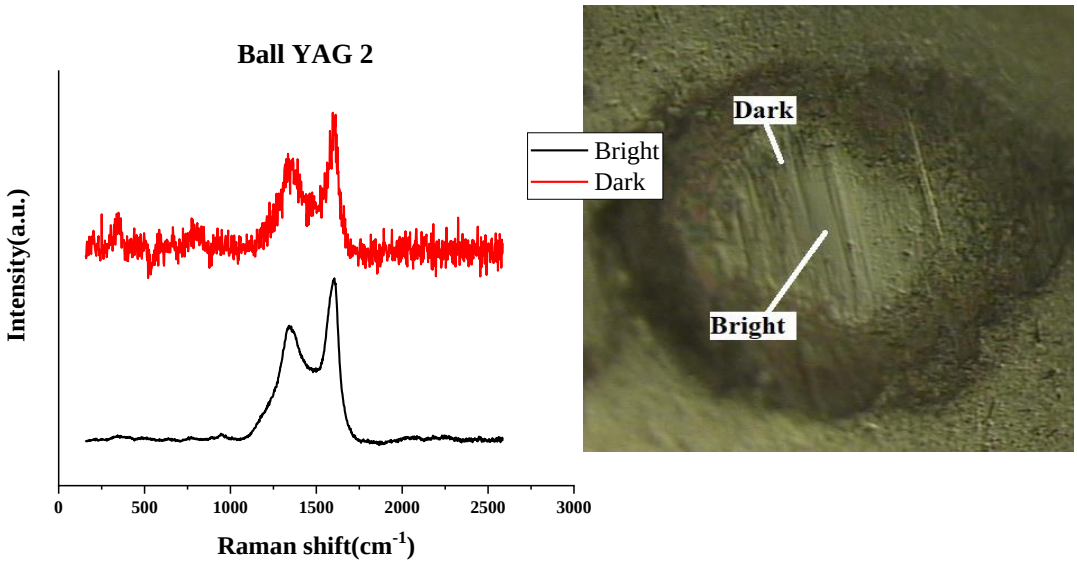

Figure 43. The Raman spectra of the ball which was in contact with YAG 2.

Finally, in case of the ball contacted YAG 3, Raman spectra, presented in Figure 44, are similar to those of in reference and WS_2 peaks as well as graphitic carbon are observable in the figure.

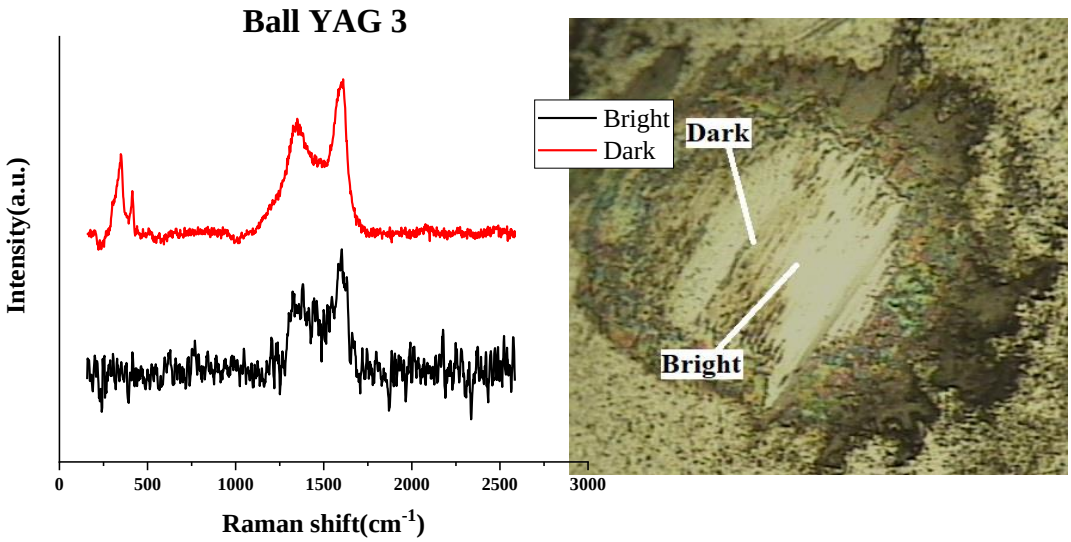

Figure 44. The Raman spectra of the ball which was in contact with YAG 3.

Chapter 5

5- Conclusion

In this work, a W-S-C coating with carbon content of ~ 50 at. % was treated by two different types of laser, namely UV and Nd:YAG ones. The coating was deposited by the DC magnetron sputtering procedure. Seven different treatment procedures were employed. Using optical microscopy, the primary investigation of the samples was done and the total affected area in each sample by the laser was estimated.

A broad peak in the diffractograms of samples has confirmed that the treated coatings still have an X-ray amorphous structure very similar to the reference. However, in the case UV 2 which was totally treated by the UV laser, there was a narrow peak at $2\theta \sim 43^{o}$ which could be attributed to Tungsten oxide carbide.

Raman spectroscopy of the samples had shown that laser treatment affected the coatings' structure and WS_2 crystallization happened in some samples. In YAG-treated samples, like YAG 1, YAG 2 and UV 1, laser power and the distance from laser focus have an important role to play in WS_2 crystallization. Either increase in laser power or decrease in the distance could result in graphitization and consequently undesirable tribological properties.

Evaluation of mechanical properties by depth-sensing nanoindentation technique confirmed that treatment can reduce the hardness of the coating in the treated zones. However, this dropping was not so significant in samples like YAG 1, YAG 2 and also, UV 1, UV 2 and UV 4; but, UV 2 and YAG 3 shown the lowest hardness, owing to over exposure.

The treatment of the coatings mainly affected the running-in and the early steady-state tribological behaviour of the coatings. The later stages of the tribological tests of the treated samples were quite similar to the reference because the treated depths were lower than depth of the wear scars.

Treatment of the sample using line and grid patterns at the selected laser power had a reverse effect on tribological properties. Graphitization of the sample could be the main reason of this behaviour.

Generally, using high power laser results in disappearing of the WS_2 and transform the C-based material. This transformation is very strong in the top, leading to graphite formation. In the bottom, power is not enough to graphitize and only the C-matrix coating remains as in the reference.

The formation of WS_2 tribofilms on the outermost surface could be introduced as the self-lubricating mechanism in the most of samples. However, graphitic carbon was also observed on the sliding surfaces, which can also provide lubricity.

References

[1] B. Bhushan, Principles and applications of tribology, John Wiley & Sons, Inc, 1999.

[2] J. A. Tichy, D. M. Meyer, Review of solid mechanics in tribology, International Journal of Solids and Structures, 37, 391-400, 2000.

[3] I. L. Singer, Friction and energy dissipation at the atomic scale: A review, Journal of Vacuum Science & Technology A, 12, 2605, 1994.

[4] T. Polcar, A. Nossa, M. Evaristo, A. Cavaleiro. Nanocomposite coatings of carbon-based and transition metal dichalcogenides phases: a review, Rev. Adv. Mater. Sci., 15, 118-126, 2007.

[5] P. L. Menezes, P. K. Rohatgi, E. Omrani, Self-Lubricating Composites, Springer Berlin Heidelberg, 2018.

[6] D. E. Newbury, J. Goldstein, J. R. Michael, Scanning Electron Microscopy and X-Ray Microanalysis, Springer, 2017.

[7] A. Jagminas, G. Niaura, R. Žalnėravičius, R. Trusovas, G. Račiukaitis, V. Jasulaitiene, Laser Light Induced Transformation of Molybdenum Disulphide-Based Nanoplatelet Arrays, Scientific Reports volume 6, 37514, 2016.

[8] S. J. An, Y. H. Kim, C. Lee, D. Y. Park, M. S. Jeong, Exfoliation of Transition Metal Dichalcogenides by a High-Power Femtosecond Laser, Scientific Reports, volume 8, 12957, 2018.

[9] J. Xia, J. Yan, Z. X. Shen, Transition metal dichalcogenides: structural, optical and electronic property tuning via thickness and stacking. FlatChem, 4, 1–19, 2017.

[10] W. Choi, N. Choudhary, G. H. Han, J. Park, D. Akinwande, Y. H. Lee, Recent development of two-dimensional transition metal dichalcogenides and their applications. Materials Today, 20(3), 116–130, 2017.

[11] T. Polcar, A. Cavaleiro, Review on self-lubricant transition metal dichalcogenide nanocomposite coatings alloyed with carbon. Surface and Coatings Technology, 206(4), 686–695, 2011.

[12] A. V. Kolobov, J. Tominaga, Two-Dimensional Transition-Metal Dichalcogenides, Springer, 2016.

[13] https://www.lowerfriction.com/product-page.php?categoryID=23.

[14] X. Duan, C. Wang, A. Pan, R. Yu, X. Duan, Two-dimensional transition metal dichalcogenides as atomically thin semiconductors: opportunities and challenges. Chemical Society Reviews, 44(24), 8859–8876, 2015.

[15] G. H. Han, D. L. Duong, D. H. Keum, S. J. Yun, Y. H. Lee, Van der Waals Metallic Transition Metal Dichalcogenides. Chemical Reviews, 118(13), 6297–6336, 2018.

[16] T. Caykara, Self-Lubricating Properties of Laser Claddings for High Temperature Forming Processes, Master thesis, Luleå University of Technology, 2018.

[17] J. K. Lancaster, A review of the influence of environmental humidity and water on friction, lubrication and wear, Tribol. Int., 23, pp. 371–389, 1990.

[18] J. V. B. Pimentel, Adaptive self-lubricating low-friction coatings. Doctoral thesis, Czech Technical University in Praque, 2013.

[19] A. Erdemir, J. Fontaine, C. Donnet, An Overview of Superlubricity in Diamond-like Carbon Films. Tribology of Diamond-Like Carbon Films, 237–262, 2008.

[20] S. Prasad, N. McDevitt, J. Zabinski, Tribology of tungsten disulfide films in humid environments: Wear, 230(1), 24–34, 1999.

[21] P. D.Fleischauer, J. R. Lince, A comparison of oxidation and oxygen substitution in MoS_2 solid film lubricants. Tribology International, 32(11), 627–636, 1999.

[22] T. Polcar, A. Cavaleiro, High-temperature tribological properties of CrAlN, CrAlSiN and AlCrSiN coatings, Surf. Coat. Technol., 206, 1244–1251, 2011.

[23] T. Polcar, Self-lubricating nanostructured coatings based on transition metal dichalcogenides alloyed with carbon. Habilitation thesis, Czech Technical University in Prague, 2009.

[24] G. Raju, Tribological study of TMD coatings for rubber applications. Master thesis, University of Coimbra, 2015.

[25] T. Polcar, M. Evaristo,, A. Cavaleiro, The tribological behavior of W-S-C lms in pin-on-disk testing at elevated temperature. Vacuum, 81(11-12):1439-1442, 2007.

[26] A. Nossa, A. Cavaleiro, Mechanical behaviour of W-S-N and W-S-C sputtered coatings deposited with a Ti interlayer. Surface and Coatings Technology, 163:552-560, 2003.

[27] B. Sigeda, The effect of N on structure, mechanical properties and tribological behaviour of TMD coatings in contact with rubber, Master thesis, University of Coimbra, 2015.

[28] P. Martin, Handbook of deposition technologies for films and coatings. Amsterdam: Elsevier, 2010.

[29] T. Polcar, M. Evaristo, A. Cavaleiro, Friction of Self-Lubricating W-S-C Sputtered Coatings Sliding Under Increasing Load, Plasma Process. Polym., 4, S541–S546, 2007.

[30] T. W. Scharf, A. Rajendran, R. Banerjee, F. Sequeda, Growth, structure and friction behavior of titanium doped tungsten disulphide (Ti-WS2) nanocomposite thin lms. Thin Solid Films, 517(19):5666-5675, 2009.

[31] G. Stachowiak, A. och Batchelor, Solid Lubricants and Surface Treatments. Engineering Tribology. Oxford: Butterworth-Heinemann, ss. 419-459, 2013.

[32] A. Erdemir, Solid lubricants and self-lubricating films. Modern Tribology Handbook. 2, 2001.

[33] D. M. Mattox, Handbook of physical vapor deposition (PVD) processing, William Andrew, 2010.

[34] C.E. Morosanu, Thin Films by Chemical Vapour Deposition, 42-43, Elsevier, 2016.

[35] S. Shahidi, B. Moazzenchi, M. Ghoranneviss, A review-application of physical vapor deposition (PVD) and related methods in the textile industry, Eur. Phys. J. Appl. Phys., 71: 31302, 2015.

[36] H. Adachi, K. Wasa, I. Kanno, H. Kotera, Handbook of sputter deposition technology. Waltham, MA: William Andrew, 2012.

[37] S. Swann, Magnetron sputtering. Physics in Technology, 19(2):67-75, 1988.

[38] P.J. Kelly, R.D. Arnell, Magnetron sputtering: a review of recent developments and applications, Vacuum 56, 159-172, 2000.

[39] J. E. Greene, Tracing the recorded history of thin-film sputter deposition: From the 1800s to 2017, Journal of Vacuum Science & Technology A 35, 05C204, 2017.

[40] O. K. Alexeeva, V. N. Fateev, Application of the magnetron sputtering for nanostructured electrocatalysts synthesis, International journal of hydrogen energy, 41 3373- 3386, 2016.

[41] G. Brue, B. Szyszka, M. Verghl, R. Bandorf, Magnetron sputtering - milestones of 30 years. Vacuum, 84(12):1354-1359, 2010.

[42] A. Nossa, A. Cavaleiro, Chemical and physical characterization of C(N)-doped W–S sputtered films. Journal of Materials Research, 19(08), 2356–2365, 2004.

[43] A. Nossa, and A. Cavaleiro. The influence of the addition of C and N on the wear behaviour of W-S-C/N coatings, Surf. Coat. Technol.142-144, 984, 2001.

[44] T. Polcar, M. Evaristo, and A. Cavaleiro. Friction of Self-Lubricating W-S-C Sputtered Coatings Sliding Under Increasing Load, Plasma Process. Polym.4, S541, 2007.

[45] E. Omrani, P. K. Rohatgi, P. L. Menezes, Tribology and Applications of Self-Lubricating Materials-CRC Press, 2018.

[46] N. Radek, K. Bartkowiak, Laser Treatment of Electro-Spark Coatings Deposited in the Carbon Steel Substrate with using Nanostructured WC-Cu Electrodes. Physics Procedia, 39, 295–301, 2012.

[47] Q. Ding, L. Wang, L. Hu, Tribology optimization by laser surface texturing: from bulk materials to surface coatings, Laser Surface Engineering, book chapter, Elsevier, 2015.

[48] T. E. Shelton, Synthesis and characterization of crystalline transition metal dichalcogenides onto stretchable substrates by laser processing, Master thesis, University of Dayton, 2015.

[49] M. G. Hudedmani, V. Soppimath, C. Jambotk, A Study of Materials for Solar PV Technology and Challenges, European Journal of Applied Engineering and Scientific Research, 5(1):1-13, 2017.

[50] J. P. Farkas, J. E. Hoopman, J. M. Kenkel, Five Parameters You Must Understand to Master Control of Your Laser/Light-Based Devices, Aesthetic Surgery Journal, 33(7) 1059 –1064, 2013.

[51] E. Kannatey-Asibu Jr, Principles of laser materials processing. John Wiley & Sons, Vol. 4, 2009.

[52] S. Kara, A. Roadmap of biomedical engineers and milestones, InTech, 2012.

[53] W. M. Steen, J. Mazumder, O. Conde, R. Villar, W. Steen, Laser Processing Surface Treatment and Film Deposition-Springer Netherlands, 1996.

[54] T. Sakamoto, M. Hasegawa, S. Kakunai, M. Ab, Laser clad lubricant layer with graphite/BN, Transactions on Engineering Sciences vol 2, 1993.

[55] V. P. Singhal, M. S. Anand, B. S. Narayan, B. M. Pande, Studies of graphite surface after laser irradiation, Bull. Mater. Sci., Vol. 20, No. 5, 719-725, 1997.

[56] A. Jagminas, G. Niaura, R. Žalnėravičius, R. Trusovas, G. Račiukaitis, V. Jasulaitiene, Laser Light Induced Transformation of Molybdenum Disulphide-Based Nanoplatelet Arrays, Scientific Reports volume 6, 37514, 2016.

[57] W. Steen, K. Watkins. Coating by laser surface treatment. Journal de Physique IV Colloque, 03 (C9), pp.C9-581-C9-590, 1993.

[58] D. Van de Wall, Laser Ablation for Advanced Surface Treatments, Laser Technik Journal, 2017.

[59] R. Eason, Pulsed Laser Deposition of Thin Films: Applications-Led Growth of Functional Materials. Wiley-Interscience, 2006.

[60] D. L. Elliott, Ultraviolet Laser Technology and Applications, Academic Press, 2014.

[61] O. Adesina, P. Popoola, O. Fatoba, Laser surface modification: A focus on the wear degradation of titanium alloy, Intech, 2016.

[62] Z. Xu, Z. He, Y. Song, X. Fu, M. Rommel, X. Luo, A. Hartmaier, J. Zhang, F. Fang, Topic Review: Application of Raman Spectroscopy Characterization in Micro/Nano-Machining, Micromachines, 9(7): 361, 2018.

[63] Y. Waseda, E. Matsubara, K. Shinoda, X-Ray Diffraction Crystallography, Springer, 2011.

[64] M. Bouroushian, T. Kosanovic, Characterization of thin films by low incidence x-ray diffraction. Crystal Structure Theory and Applications, 1(3):35-39, 2012.

[65] F. Gustavsson, Triboactive component coatings. Tribological testing and microanalysis of low-friction triboflms. Doctoral thesis, Uppsala University, 2013.

[66] C. A. Schuh, Nanoindentation studies of materials, Vol. 9, Issue 5, 32-40, 2006.

[67] J. Antunes, A. Cavaleiro, L. Menezes, M. Simões, J. Fernandes, Ultra-microhardness testing procedure with Vickers indenter. Surface and Coatings Technology, 149(1), 27–35, 2002.

[68] K. Holmberg, A. Matthews, Coatings Tribology, Second Edition: Properties, Mechanisms, Techniques and Applications in Surface Engineering, Elsevier Science, 2009.

[69] Y. Waseda, E. Matsubara, K. Shinoda, X-Ray Diffraction Crystallography, Springer, 2011.

[70] A. C. Ferrari, J. Robertson, Interpretation of Raman spectra of disordered and amorphous carbon. Physical Review B, 61(20), 14095–14107, 2000.

[71] A. Berkdemir, H. R. Gutiérrez, A. R. Botello-Méndez, N. Perea-López, A. L. Elías, Chen-Ing Chia, B. Wang, V. H. Crespi, F. López-Urías, J. C. Charlier, H. Terrones, M. Terrones, Identification of individual and few layers of WS_2 using Raman Spectroscopy. Sci. Rep. 3, 1755, 2013.

[72] L. wang, Y. wang, Y. cheng, Z. Liu, Q. guo, M. N. Ha and Z. Zhao, Hydrogen-treated mesoporous WO3 as a reducing agent of CO2 to fuels (CH4 and CH3OH) with enhanced photothermal catalytic performance, J. Mater. Chem. A, 2016.